Ore Geology Reviews 162 (2023) 105676

Contents lists available at ScienceDirect

Ore Geology Reviews

journal homepage: www.elsevier.com/locate/oregeorev

Origin and mineralization processes of REE during magmatic-hydrothermal evolution: Insights from in-situ geochemistry of calcite from the Weishan REE deposit, eastern North China Craton

Lang-Ye Zhao [a,b], Ting-Guang Lan [a,b,*], Hong-Rui Fan [c], Jun Lan [d], Hong Wang [a], Wei Terry Chen [a,b], Huan-Long Hu [a], De-Jian Li [e]

[a] State Key Laboratory of Ore Deposit Geochemistry, Institute of Geochemistry, Chinese Academy of Sciences, Guiyang 550081, China
[b] College of Earth and Planetary Sciences, University of Chinese Academy of Sciences, Beijing 100049, China
[c] Key Laboratory of Mineral Resources, Institute of Geology and Geophysics, Chinese Academy of Sciences, Beijing 100029, China
[d] The Fifth Geological Brigade, Shandong Provincial Bureau of Geology & Mineral Resources, Tai'an 271000, China
[e] Shandong Weishan REE Co Ltd, Weishan 277600, China

ARTICLE INFO

Keywords:
LA-ICP-MS
Calcite
Magmatic-hydrothermal evolution
REE mineralization
Weishan REE deposit

ABSTRACT

The Weishan REE deposit, hosting more than one million tons of light REE oxides ($LREE_2O_3$), is one of the largest LREE deposits in China. It has been considered to be a carbonatite-related REE deposit, but whether carbonatites occurred or not is still controversial, leading to the confusions of how the LREE originated and mineralized. Here, we conducted in-situ elemental and Sr-Nd isotopic analyses on different stages of calcite from the Weishan REE deposit, combined with petrographic and bulk C-O isotopic studies, with the aim to unravel the origin and mineralization processes of REE. Four stages of calcite (Cal-1, Cal-2, Cal-3 and Cal-4) were identified, of which the Cal-1 typically coexists with K-feldspar and quartz while the Cal-2 and Cal-3 coexist with sulfates and REE minerals (e.g., bastnäsite and parisite), respectively. The Cal-4 occurs in the post-ore veinlets and coexists with sulfides. The Cal-1 is characterized by exsolution of carbocernaite along its cleavage planes with highest Na, K, Sr, Ba and LREE contents. The other stages of calcite show continuous decrease of the above elements. Combined with petrographic features and elemental discrimination diagrams, it is concluded that the Cal-1 is magmatic while the others are hydrothermal. These calcites thus indicate a continuous magmatic-hydrothermal evolution. The four stages of calcite show similar isotopic compositions, which are consistent with those of the alkaline silicate rocks in the ore district, suggesting an uniform source or magma chamber for their derivation. Considering the magmatic features of Cal-1, it is inferred that carbonate melts coupled with abundant alkaline fluids were exsolved from the alkaline magmas. Alkalis (e. g., K and Na) were enriched in the magmatic-hydrothermal system with potassic metasomatism being more prevalent, which might play an important role in REE exsolution and transportation. Focused REE deposition occurred shortly after massive deposition of sulfates, indicating that REE-sulfate complexes might be the dominant transporting ligands of REE. The deposition of REE was mainly induced by fluid boiling, as indicated by the boiling/unmixing features of fluid inclusions. The Sr-Nd isotopic compositions of ores and associated alkaline rocks show affinities to the enriched lithospheric mantle (EM) beneath the study region, but are more depleted. Because subduction of the Paleo-Pacific oceanic plate beneath the eastern Asian occurred since the Jurassic, it is inferred that CO_2- and REE-rich melts/fluids released from the subducted oceanic slab metasomatized the EM, leading to a REE-rich carbonated mantle. Rollback of the subducted slab occurred during the early Cretaceous, resulting in partial melting of the EM and thus generating the CO_2- and REE-rich alkaline magmas. This deposit shows significant hydrothermal features with poorly-developed carbonatites, distinct from the typical carbonatite-related REE deposits in the other places. The REE mineralization is thus considered to be basically controlled by the alkaline magmas rather than the carbonatites.

* Corresponding author at: Institute of Geochemistry, Chinese Academy of Sciences, No.99 Linchengxi Road, Guiyang, Guizhou Province 550081, China.
E-mail address: lantingguang@mail.gyig.ac.cn (T.-G. Lan).

https://doi.org/10.1016/j.oregeorev.2023.105676
Received 10 July 2023; Received in revised form 12 September 2023; Accepted 14 September 2023
Available online 19 September 2023

1. Introduction

Carbonatite-related REE deposits are one of the most important types of REE deposits, which account for >50% of the global REE resources (total rare earth oxides plus yttrium oxide, REY) (Weng et al., 2015). It is also the dominant type of REE deposits in China, hosting about 97% of the China's REE resources (Xie et al., 2019). The Weishan REE deposit, accounting for about 1 million tons of light REE (LREE) oxides (Zhang et al., 2022), has been considered to be one of the largest carbonatite-related LREE deposit in China (Xie et al., 2019). However, this deposit is typically hosted by alkaline rocks and Precambrian metamorphic rocks, showing REE-bearing quartz-sulfate-carbonate veins with significant hydrothermal features (Yu et al., 2010; Lan et al., 2011b; Wang et al., 2016). Although calcite is common, whether magmatic calcite occurred or not is still controversial. Different views have been proposed for the genesis of the calcite: (1) crystallization from carbonate melts immiscible with alkaline silicate melts (e.g., Li et al., 2009; Wang et al., 2019); (2) deposition from alkaline magma-derived magmatic-hydrothermal fluids (e.g., Yu et al., 2010; Lan et al., 2011b). Because the REE minerals are closely associated with the calcite, the above controversies lead to the confusions of how the REE originated and precipitated. Some researchers considered that the REE was derived from the carbonate melts and thus precipitated at the magmatic or magmatic-hydrothermal transition stages (Li et al., 2009; Wang et al., 2019), whereas the others believed that the REE was derived from the alkaline magmas and precipitated in the hydrothermal fluids (Lan et al., 2011b; Wang et al., 2016; Jia and Liu, 2020). In summary, the genesis of the calcite and the mineralization mechanisms of the REE remain unclear, hindering further exploration and exploitation.

Multiple generations of calcite have been identified in the Weishan REE deposit (Wang et al., 2019), which show coexistence with different minerals such as K-feldspar, quartz, sulfates, carbonates, fluorides and sulfides. Fluid inclusions in the coexistent quartz have homogenization temperatures varying widely from ~ 550℃ to ~ 150℃ (Li et al., 2009; Lan et al., 2011b), indicating that the calcite might record the magmatic-hydrothermal processes. In addition, it has been shown that the elemental and isotopic compositions of carbonates can effectively trace the genesis of REE mineralization (e.g., Xu et al., 2010; Chakhmouradian et al., 2016; Yang et al., 2019a, Chen et al., 2020b; Gao et al., 2021). In this contribution, in-situ elemental and Sr-Nd isotopic analyses on different stages of calcite from the Weishan REE deposit were conducted, combined with detailed petrographic and bulk C-O isotopic studies, with the aim to unravel the origin and mineralization processes of REE.

2. Geological setting

2.1. Regional geology

The Weishan REE deposit is located at the southern Luxi Block, eastern North China Craton (NCC; Fig. 1a). The NCC is the largest and oldest craton in China (Zhai and Santosh, 2011), which is mainly constituted by a basement with Archean to Paleoproterozoic tonalitic-trondhjemitic-granodioritic (TTG) gneisses and greenschist to granulite facies volcano-sedimentary rocks and a cover with Mesoproterozoic

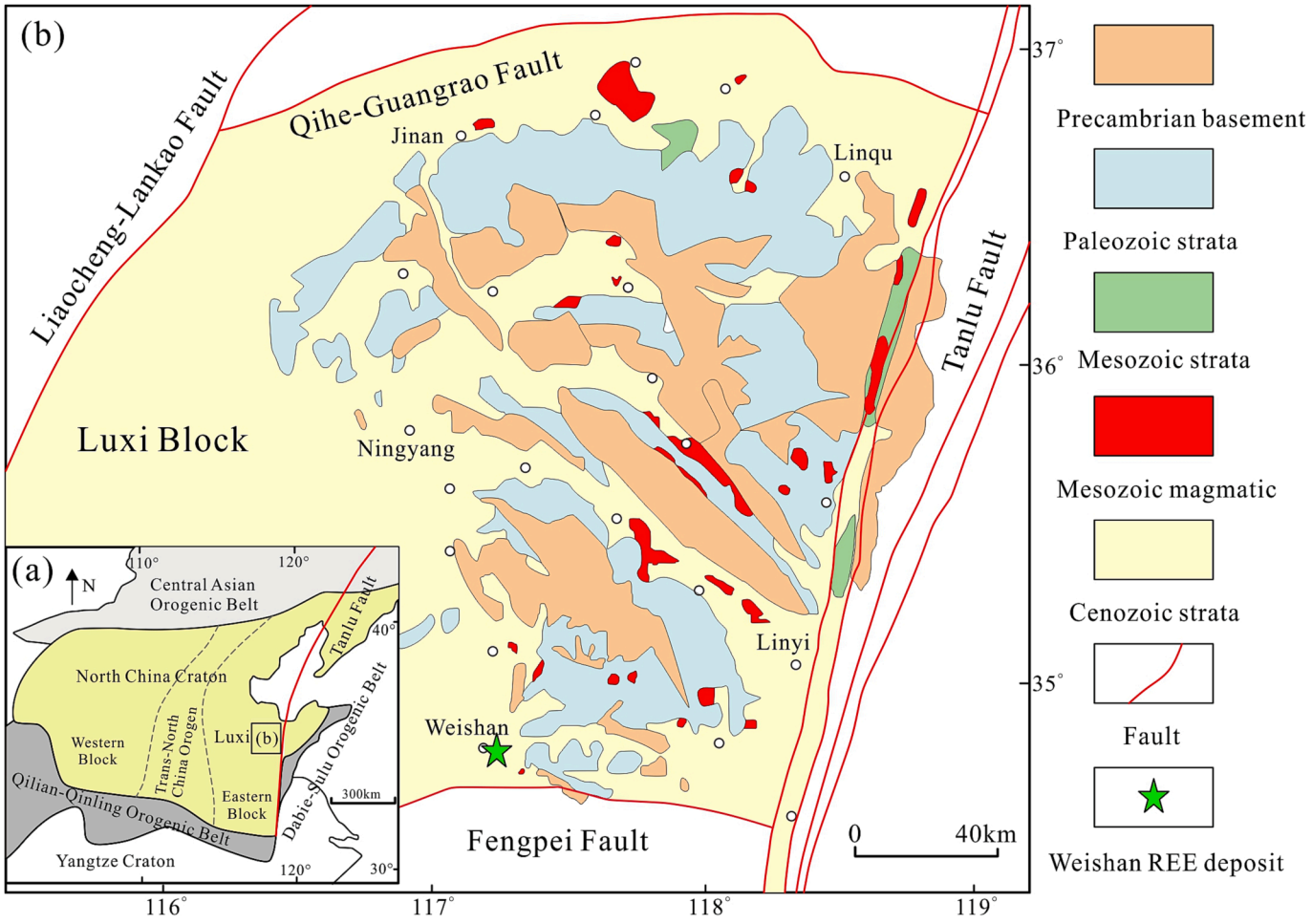

Fig. 1. Tectonic subdivision of the North China Craton with the location of Luxi Block (a) and simplified geological map of the Luxi Block (b). (a) and (b) are modified after Zhang et al. (2005) and Zhang et al. (2007), respectively.

to Neoproterozoic volcano-sedimentary rocks, Cambrian to Ordovician epicontinental carbonate rocks, Carboniferous to Permian alternating marine and terrestrial sequences and Mesozoic-Cenozoic basin sediments (Lu et al., 2008). The craton was suffered remarkable destruction at its central-eastern domains since the Mesozoic (Zhu et al., 2012), where >120 km Archean lithosphere was lost (Fan et al., 2000), inducing large-scale magmatic activities and various mineralizations (e.g., Au, Fe and Cu deposits) (Li and Santosh, 2014). The Luxi Block is located at the eastern domain of the NCC, which is bounded by the Tanlu fault in the east, the Qihe-Guangrao fault in the north, the Liaocheng-Lankao fault in the west and the Fengpei fault in the south (Fig. 1b). The Tanlu fault extended deeply into the mantle, not only acting as a conduit for asthenospheric upwelling (Chen et al., 2006), but also controlling the emplacement of widespread Mesozoic igneous rocks in the Luxi Block (Qiu et al., 2000; Ren et al., 2002). All kinds of igneous rocks, such as gabbros, high-Mg diorites, high-K calc-alkaline to alkaline rocks, granites, basaltic to rhyolitic volcanic rocks, carbonatites and mafic dykes occurred in this region during the Mesozoic (Lan et al., 2019). The alkaline rocks are represented by the early Jurassic Tongshi intrusive complex in the Pingyi county, the early Cretaceous Longbaoshan complex in the Cangshan county and the Chishan complex in the Weishan county (Lan et al., 2011a, 2011b, 2012; Ding et al., 2022), which were prone to generate Au and REE deposits.

2.2. Deposit geology

The Weishan REE deposit is located at the southeast of the Weishan county, southern Luxi Block, which is closely associated with the Weishan alkaline complex (Fig. 1b). The Weishan alkaline complex contains quartz syenite, alkaline granite and aegirine quartz syenite porphyry, of which the quartz syenite is dominant (Fig. 2). These rocks intruded into the late Archean gneisses with the ages of 119–130 Ma (Liang et al., 2017; Wei et al., 2019; Ding et al., 2022). Orebodies mainly occur as NW-NE trending veins in the quartz syenite and gneisses (Figs. 2 and 3a, b). Available geochronological studies using Rb-Sr, Re-Os and U-Th-Pb dating show that the REE mineralization formed at 119–122 Ma (Lan et al., 2011b; Yang et al., 2019b; Zhang et al., 2023), generally consistent with those of the host alkaline rocks. The REE oxide (RE_2O_3) grades commonly vary from 1.5 wt% to 7.5 wt% (Zhang et al., 2022), with some high-grades up to 10–18 wt% (Wang et al., 2016).

The orebodies are mainly composed of carbonates (mainly calcite), sulfates (e.g., barite and celestite), LREE minerals (mainly bastnäsite and parisite), quartz, fluorite and sulfides (e.g., pyrite, sphalerite and galena). Based on crosscutting relationships of veins and mineral assemblages, four major paragenetic sequences can be identified in this deposit from the early to the late stages: (1) K-feldspar + quartz + calcite, (2) sulfate + quartz + calcite, (3) REE mineral + quartz + calcite + sulfate + fluorite and (4) post-ore calcite + quartz + fluorite + sulfide stages. The stage 1 is characterized by coarse-grained calcite (Cal-1) and quartz with minor K-feldspar (Fig. 3c). The stage 2 is composed of coarse-grained calcite (Cal-2), massive barite, celestite and quartz (Fig. 3d). The stage 3 is characterized by abundant bastnäsite and parisite coexisting with fine-grained calcite (Cal-3) and sulfates (Fig. 3d–f). Other minerals such as fluorite and muscovite are also common in this stage. The stage 4 shows veinlets composed of calcite (Cal-4), quartz, fluorite and sulfides such as pyrite, chalcopyrite, sphalerite and galena (Fig. 3e, f). The paragenetic sequences and mineral assemblages are summarized in Fig. 4.

3. Sampling and methods

Sixty-three samples were collected from the ore veins of No.12 (N =

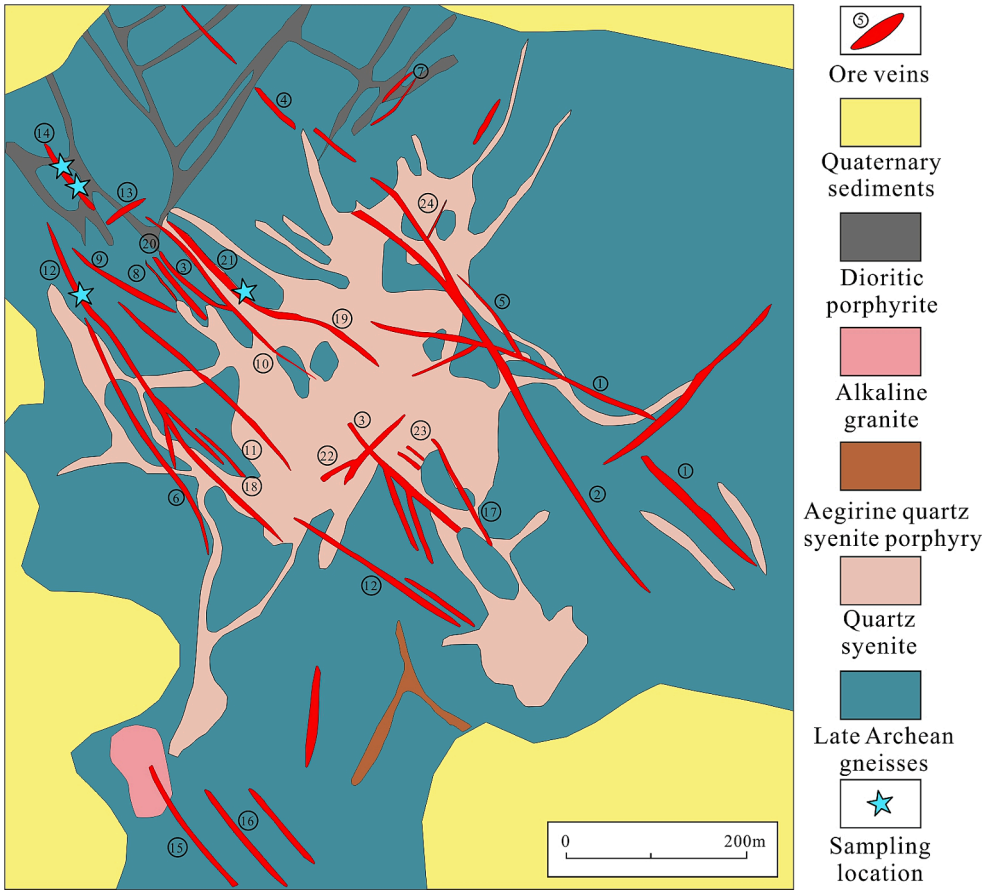

Fig. 2. Geological map of the Weishan REE deposit (modified after Zeng et al., 2022).

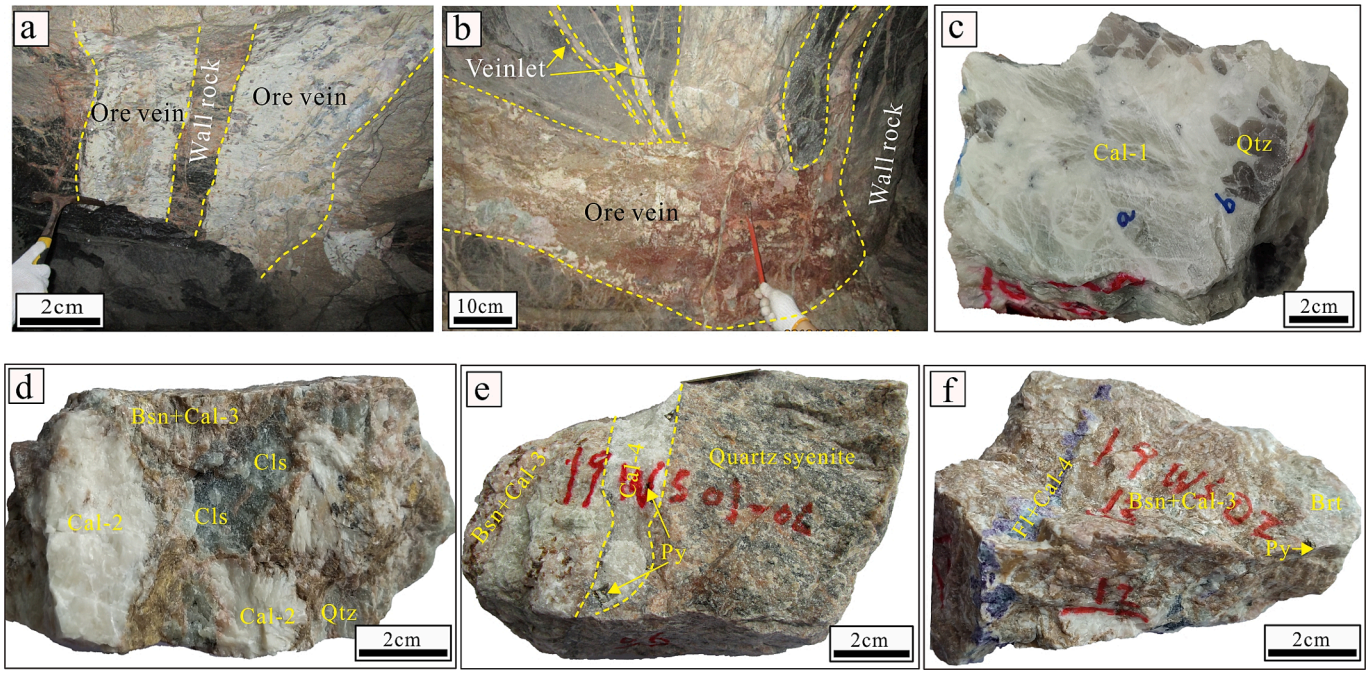

Fig. 3. Ore veins and hand specimens of different stages of calcite from the Weishan REE deposit. (a) Ore veins cutting the altered alkaline rock. (b) Ore veins cutting the late Archean metamorphic rock. (c) Coarse-grained stage 1 calcite (Cal-1, light green) showing coexistence with coarse quartz. (d) Coarse-grained stage 2 calcite (Cal-2, white) coexisting with celestite, cut/metasomaztized by stage 3 calcite (Cal-3, brown) and bastnäsite. (e) Fine-grained stage 3 calcite coexisting with bastnäsite, cut by stage 4 calcite (Cal-4, white) vein. (f) Stage 4 calcite + fluorite (purple to light green) veinlet cutting stage 3 calcite + bastnäsite. Abbreviations: Cal = calcite; Qtz = quartz; Bsn = bastnäsite; Brt = barite; Cls = celestite; Fl = fluorite; Py = pyrite.

Mineral \ Stage	Stage 1	Stage 2	Stage 3	Stage 4
Aegirine-augite				
K-feldspar				
Quartz				
Apatite				
Calcite	Cal-1	Cal-2	Cal-3	Cal-4
Carbocernaite				
Barite				
Celestite				
Bastnasite				
Parisite				
Fluorite				
Monazite				
Strontianite				
Pyrite				
Chalcopyrite				
Sphalerite				
Galena				

Fig. 4. Summary of paragenetic sequences and mineral assemblages of different stages from the Weishan REE deposit.

19), No.14 (N = 29) and No.21 (N = 15) at the mining tunnels of the Weishan REE deposit (Fig. 2). Two Paleozoic limestone samples (sedimentary calcite) were collected from the Laiwu area of the Luxi Block for comparative study. The samples were prepared into polished thin sections (~100 μm) for mineralogical and geochemical analyses by scanning electron microscope (SEM), electron probe microanalyzer (EPMA), laser ablation-inductively coupled plasma mass spectrometer (LA-ICP-MS) and laser ablation-multiple collector inductively coupled plasma mass spectrometer (LA-MC-ICP-MS). Some powder samples of calcite were also prepared for isotope ratio mass spectrometer (IRMS) analysis. All the analyses were conducted at the State Key Laboratory of Ore Deposit Geochemistry, Institute of Geochemistry, Chinese Academy of Sciences.

3.1. BSE and CL imaging

Back-scattered electron (BSE) and cathodoluminescence (CL) images of minerals were acquired to check the microtextures and mineral assemblages. The BSE imaging was conducted by a JEOL JSM–7800F field emission SEM. The working conditions were 20 kV accelerating voltage and 10nA beam current. The CL imaging of calcite was conducted by a Reliotron luminoscope (type HC1–LM) attached to a polarization microscope and digital camera. The CL images were captured at 5–10 kV acceleration voltage and 0.5 mA beam current.

3.2. EPMA analysis

The major element compositions of calcite were determined by a JEOL JXA8530F-plus EPMA. The working conditions were 15 kV accelerating voltage, 10nA beam current and 5 μm beam spot. The peak counting time was 10 s for Ca, Ba, Fe, Mn, Na, Sr and Mg. Data was corrected on-line using a ZAF procedure. The standards used for calibration processes include calcite (Ca), benitoite (Ba), pyrope (Fe, Mg and Mn), plagioclase (Na) and anhydride (Sr).

3.3. LA-ICP-MS trace element analysis and mapping

The in-situ trace element compositions of calcite were analyzed using a GeolasPro 193 nm laser ablation system attached to an Agilent 7900 ICP-MS. The contents of Ca determined by EMPA were used as internal standard, and the glass NIST 612 was used as external standard for calibration. The carbonate standard MACS-3 was analyzed to monitor the accuracy, which shows that most of the analyzed elements have the accuracies better than 10%. Each analysis consists of approximately 30 s background acquisition, followed by 60 s sample data acquisition. Laser spot size of 44 μm, repetition rate of 5 Hz and fluence of 4 J/cm^2 were used during the analyses.

The LA-ICP-MS elemental mapping was performed using a RESOlution 193 nm laser ablation system attached to an Agilent 7700X ICP-MS. Pre-selected areas were ablated by defining a number of equally spaced lines. In this study, lines were ablated using the laser spot size of 10 μm, repetition rate of 10 Hz, fluence of 3 J/cm^2 and scanning speed of 7 μm/s. The glass NIST 610 was used for calibration. Processing and imaging of the data were done using the *Iolite* software (Paton et al., 2011).

3.4. LA-MC-ICP-MS Sr-Nd isotopic analyses

The in-situ Sr-Nd isotopic analyses of calcite were conducted using a RESOlution-155 ArF 193 nm laser ablation system attached to a Nu Plasma III MC-ICP-MS. Helium was used as the carrier gas, with a flow of 200 ml/min. Each analysis incorporated a background acquisition of approximately 30 s followed by 40 s data acquisition from the sample. Uniformed repetition rate of 6 Hz and fluence of 5 J/cm^2 were used during the analyses, but different spot sizes were used for the Sr (26–60 μm) and Nd (60–228 μm) isotopes, depending on the Sr and Nd contents of the samples. The analyses followed the standard-sample bracketing procedure, in which an external standard was repeatedly measured every five unknown samples for mass bias correction while one or two monitor standards were measured every fifteen samples for quality control. The isotopic ratios were corrected for mass fractionation by normalizing to $^{86}Sr/^{88}Sr = 0.1194$ and $^{146}Nd/^{144}Nd = 0.7219$, respectively. The correction protocols can be seen in Yang et al. (2014) and references therein. For the Sr isotopic analysis, the modern-day coral (Chen et al., 2018) was analyzed for mass bias correction, while the apatite standard MAD (Yang et al., 2014) was analyzed to monitor the analytical precision. The repeated analyses of the MAD in this study yielded an average $^{87}Sr/^{86}Sr$ ratio of 0.711710 ± 64 (2σ), which is consistent with the recommended value of 0.711798 ± 26 within errors (Yang et al., 2014). For the Nd isotopic analysis, the MAD was analyzed for mass bias correction, while the AP2 was analyzed to monitor the analytical precision. The repeated analyses of AP2 yielded an average $^{143}Nd/^{144}Nd$ ratio of 0.511019 ± 24 (2σ), which is also consistent with the recommended value of 0.511007 ± 30 within errors (Yang et al., 2014).

3.5. IRMS C-O isotopic analyses

A total of 19 calcite powders were selected for C-O isotopic analyses. Calcite powders were in-situ collected on hand specimens using a micro-drilling system (RELION MSS VI). The powders reacted with phosphoric acid at 72 °C for at least 4 h to generate CO_2, which were then analyzed by MAT-253 IRMS for C-O isotopic compositions. The $\delta^{13}C$ and $\delta^{18}O$ values were expressed against V-PDB. The $\delta^{18}O_{PDB}$ was converted to $\delta^{18}O_{SMOW}$ using the formula of $\delta^{18}O_{SMOW} = 1.03091 \times \delta^{18}O_{PDB} + 30.91$ (Coplen et al., 1983). The reference standards of GBW04405, GBW04416, IAEA-603 and IAEA-CO-8 were used as external standards, which show the analytical precisions for the C-O isotopic compositions better than ± 0.2‰.

4. Results

4.1. Petrography and microtexture of calcite

The four stages of calcite (Cal-1, Cal-2, Cal-3 and Cal-4) show different petrographical and microtextural features. The Cal-1 grains coexist with K-feldspar and quartz, which are commonly coarse and euhedral to subhedral (Fig. 3c and 5a). Under the BSE imaging, they show well-developed cleavage fractures, along which large amounts of carbocernaite lamellas are distributed (Fig. 5b). The Cal-2 grains coexist with quartz and sulfates such as barite and celestite (Fig. 3d). They are also coarse-grained with well-developed cleavages (Fig. 5c). The Cal-3 grains are fine-grained and anhedral without clear cleavages (Fig. 5c), cutting the Cal-2 with different color and distinct boundaries under the CL and BSE imaging (Fig. 5d, e). They typically coexist with REE minerals such as bastnäsite and parisite (Fig. 5f, g). Notably, the bastnäsite and parisite are commonly coarse-grained and euhedral (Fig. 5f, g), which are intergrown with each other (Fig. 5h, i). The Cal-4 grains occur in the post-ore veinlets and are fine-grained with anhedral shape (Fig. 5j). They are commonly clean under the BSE imaging (Fig. 5k).

4.2. Major and trace elements of calcite

The elemental contents of different stages of calcite vary widely, especially the Cal-1 shows distinct features from the others. Major elements analyzed by EPMA show that the CaO contents are the lowest in the Cal-1 (38.5–50.6 wt%), while those of the Cal-2 (50.2–55.5 wt%), Cal-3 (50.2–55.8 wt%) and Cal-4 (51.6–56.6 wt%) are generally comparable (Supplementary Table S1). The Cal-1 also has the lowest MnO (<0.7 wt%) and highest SrO contents (up to ~ 11 wt%), while the others commonly have the MnO and SrO contents of 1–4 wt% (Fig. 6a). Other elemental contents are generally lower than 1 wt%. The LA-ICP-MS analytical results show that Na, Mn, Fe, Mg, Sr, Ba and ∑REE are the

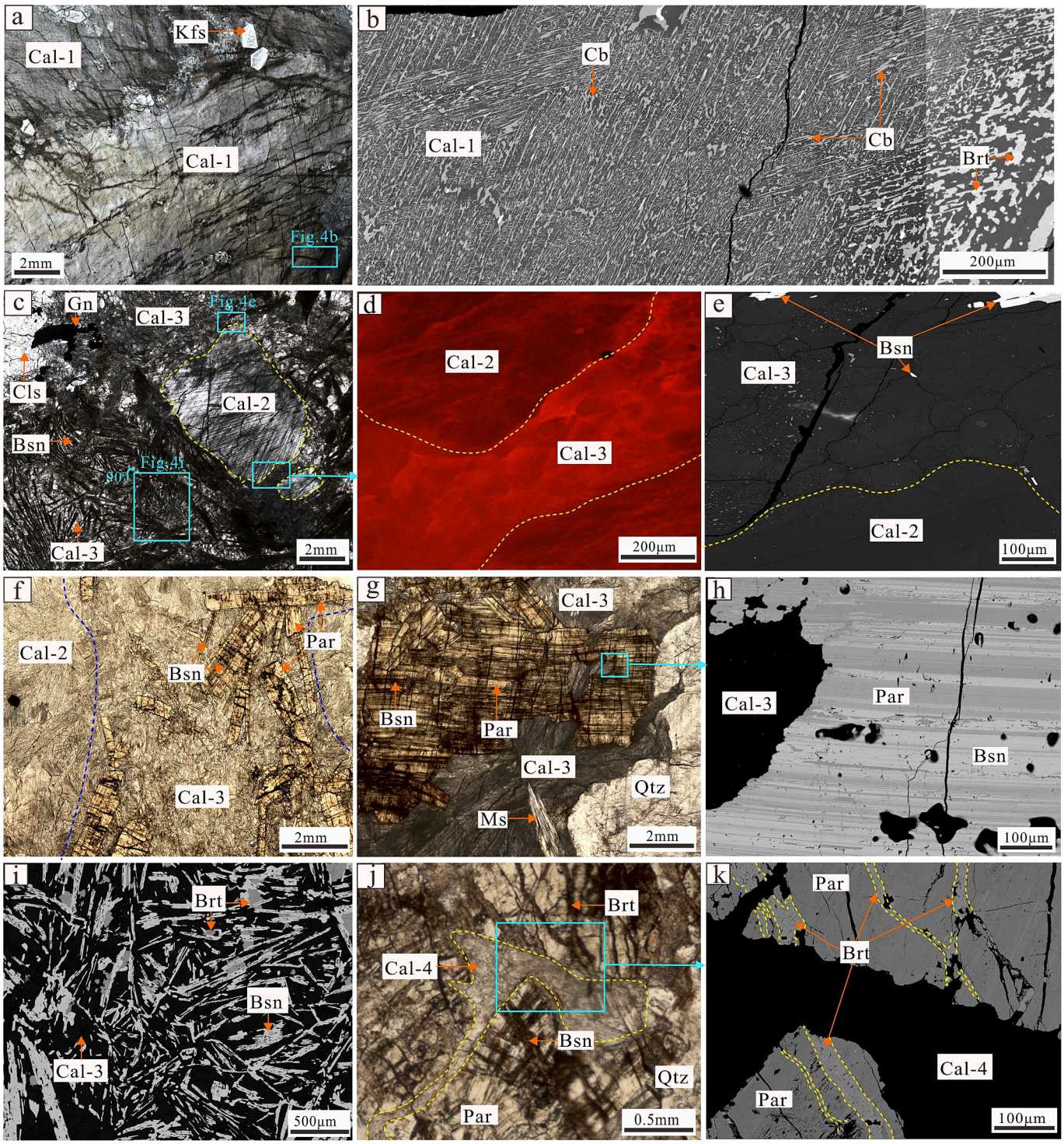

Fig. 5. Micrographs showing mineral assemblages and microtextures of different stages of calcite from the Weishan REE deposit. (a) Coarse-grained Cal-1 coexisting with K-feldspar. (b) Carbocernaite distributing along cleavage planes of Cal-1. (c) Coarse-grained Cal-2 (with obvious cleavages) residing in fine-grained Cal-3. (d) Cal-3 cutting Cal-2 with clear boundary. (e) Cal-3 containing numerous mineral inclusions and cutting Cal-2. (f) Cal-3 coexisting with coarse-grained euhedral REE minerals (bastnäsite and parisite) and cutting Cal-2. (g, h) Cal-3 coexisting with intergrown bastnäsite and parisite. (i) Cal-3 coexisting with acicular bastnäsite and minor barite. (j, k) Fine-grained Cal-4 cutting parisite and barite. (a), (c), (f), (g) and (j) are under transmitted light. (b), (e), (h), (i) and (k) are BSE images. (d) is CL image. Abbreviations: Kfs = K-feldspar; Cal = calcite; Qtz = quartz; Ms = muscovite; Cb = carbocernaite; Brt = barite; Cls = celestite; Bsn = bastnäsite; Par = parisite; Gn = galena; Py = pyrite.

most abundant trace elements in all the calcite, showing contents up to hundreds to tens of thousands of ppm (Supplementary Table S2). Potassium, Y and Pb are less abundant, showing tens to hundreds of ppm. Other elements such as Cu, Zn and Ga show several to tens of ppm. Specifically, the Cal-1 has the lowest Mg (128–1770 ppm), Fe (191–613 ppm) and Mn (2130–4870 ppm) but the highest Na (687–12300 ppm), K (36.5–665 ppm), Zn (4.71–32.3 ppm), Ga (10.7–129 ppm), Pb (63.5–529 ppm), Sr (66200–175000 ppm) and Ba (7410–127000 ppm) contents among the studied calcites. Most of the trace elements in Cal-4, especially the Sr (479–17700 ppm) and Ba (0.22–2110 ppm), show the

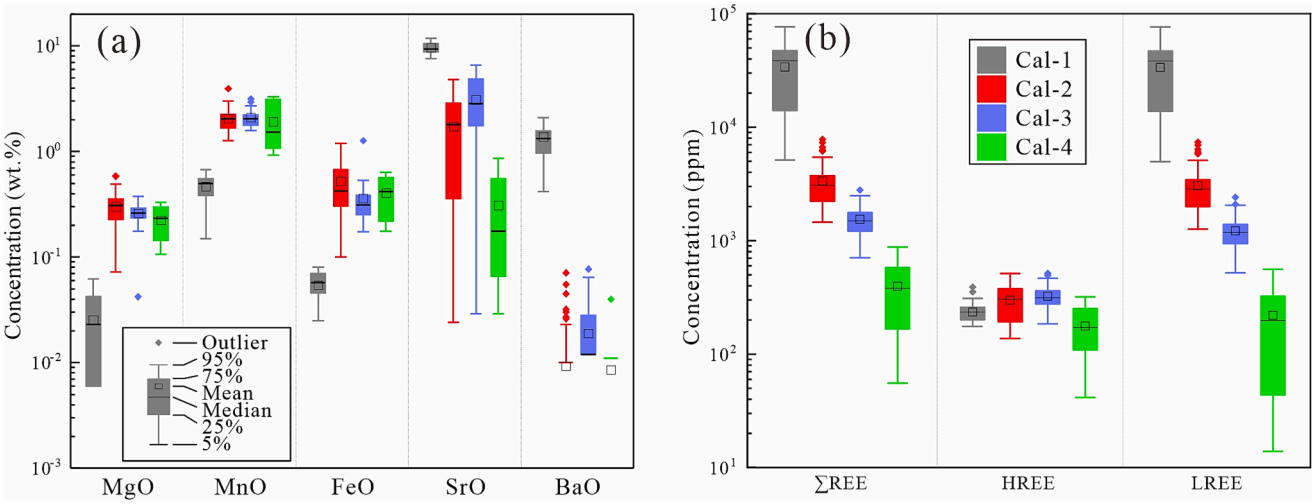

Fig. 6. Summary and comparison of major element (a) and REE (b) concentrations for different stages of calcite from the Weishan REE deposit. The detailed data are listed in Supplementary Table S1 and Table S2, respectively.

lowest contents. The trace elemental contents of Cal-2 and Cal-3 commonly vary between those of the Cal-1 and Cal-4. The LREE as well as the ∑REE contents show a continuous decrease from the Cal-1 to Cal-4, but the HREE contents do not change too much, leading to the decreasing fractionation between the LREE and HREE (Fig. 6b and 7). For example, the $(La/Yb)_N$ ratios in Cal-1, Cal-2, Cal-3 and Cal-4 are 88–2440 (mean of 996), 4.85–44.9 (mean of 16.2), 1.04–7.72 (mean of 3.36) and 0.08–0.81 (mean of 0.43), respectively. The $(La/Yb)_N$ ratios

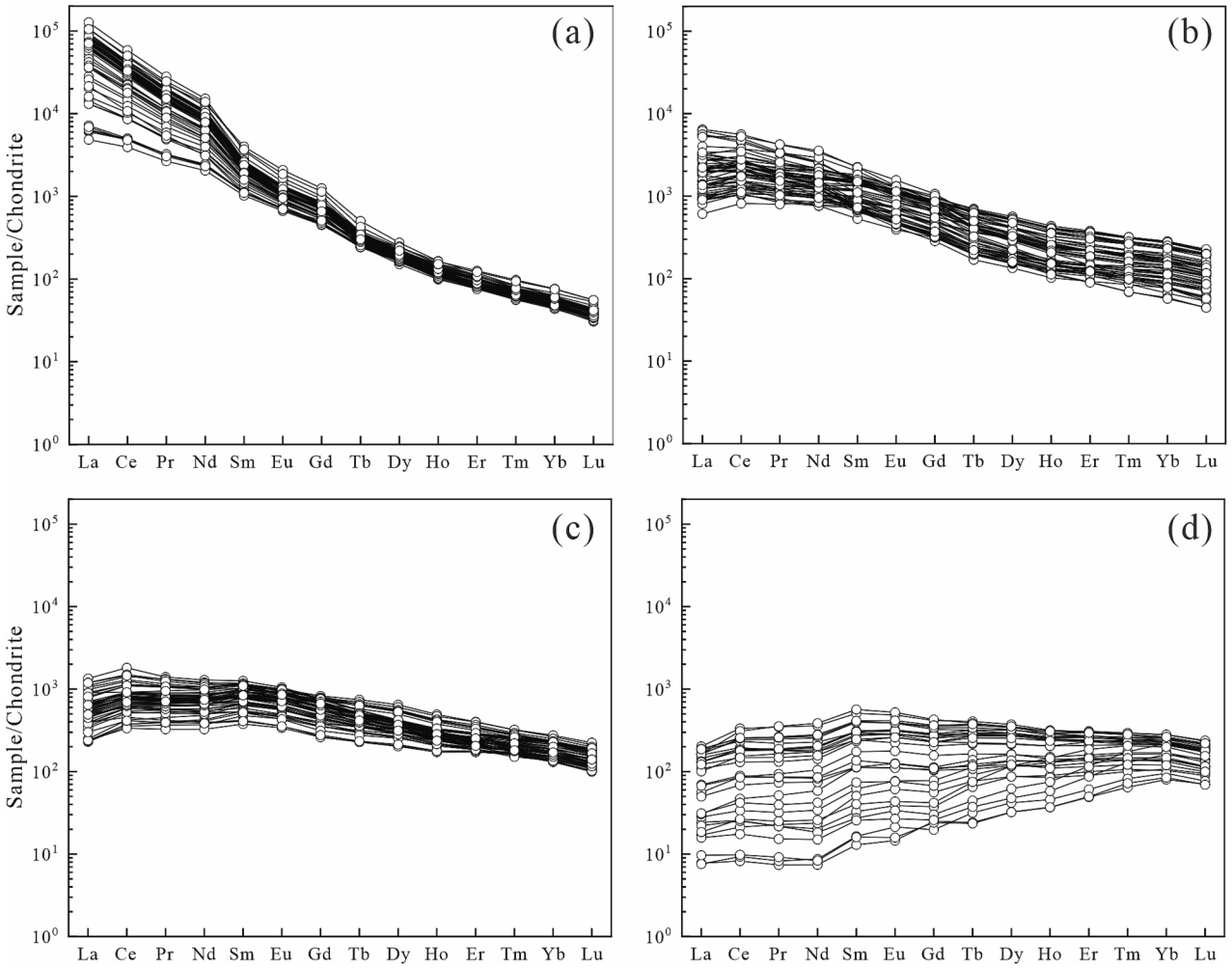

Fig. 7. Chondrite-normalized REE distribution patterns for Cal-1 (a), Cal-2 (b), Cal-3 (c) and Cal-4 (d) from the Weishan REE deposit. Chondrite values are from Sun and McDonough (1989).

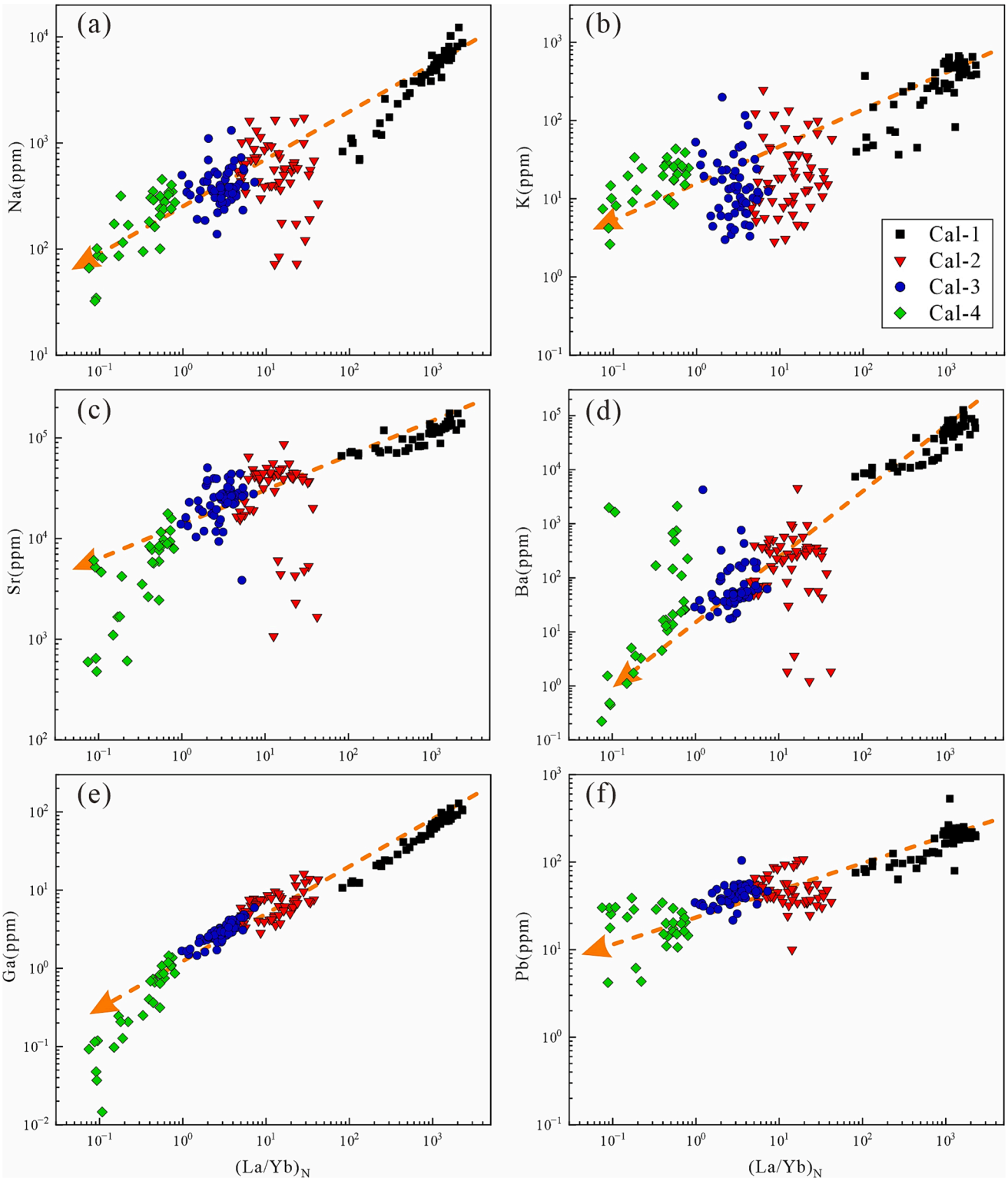

Fig. 8. Covariant plots for different elements vs. $(La/Yb)_N$ ratio in calcite. The $(La/Yb)_N$ is chondrite-normalized and the arrows indicate the trends from the early to the late stages.

are generally positively correlated with the Na, K, Sr, Ba, Ga and Pb contents (Fig. 8).

LA-ICP-MS mapping shows that the distributions of Ca, Sr and Ba in Cal-1 are well consistent with the rhythmic zoning of the calcite, while the Na, K and LREE (e.g., Ce) show consistent behaviors along fractures or latter modification (Fig. 9). The HREE (e.g., Y) shows distinct distribution from the above elements, which seems to be neither correlated with the rhythmic zoning nor with the latter fractures (Fig. 9).

4.3. Sr-Nd isotopic compositions of calcite

The $^{87}Sr/^{86}Sr$ and $^{143}Nd/^{144}Nd$ ratios of the studied calcites vary from 0.707330 to 0.708974 and 0.511725 to 0.512352, respectively (Supplementary Table S3). Based on the mineralization age of 122 Ma

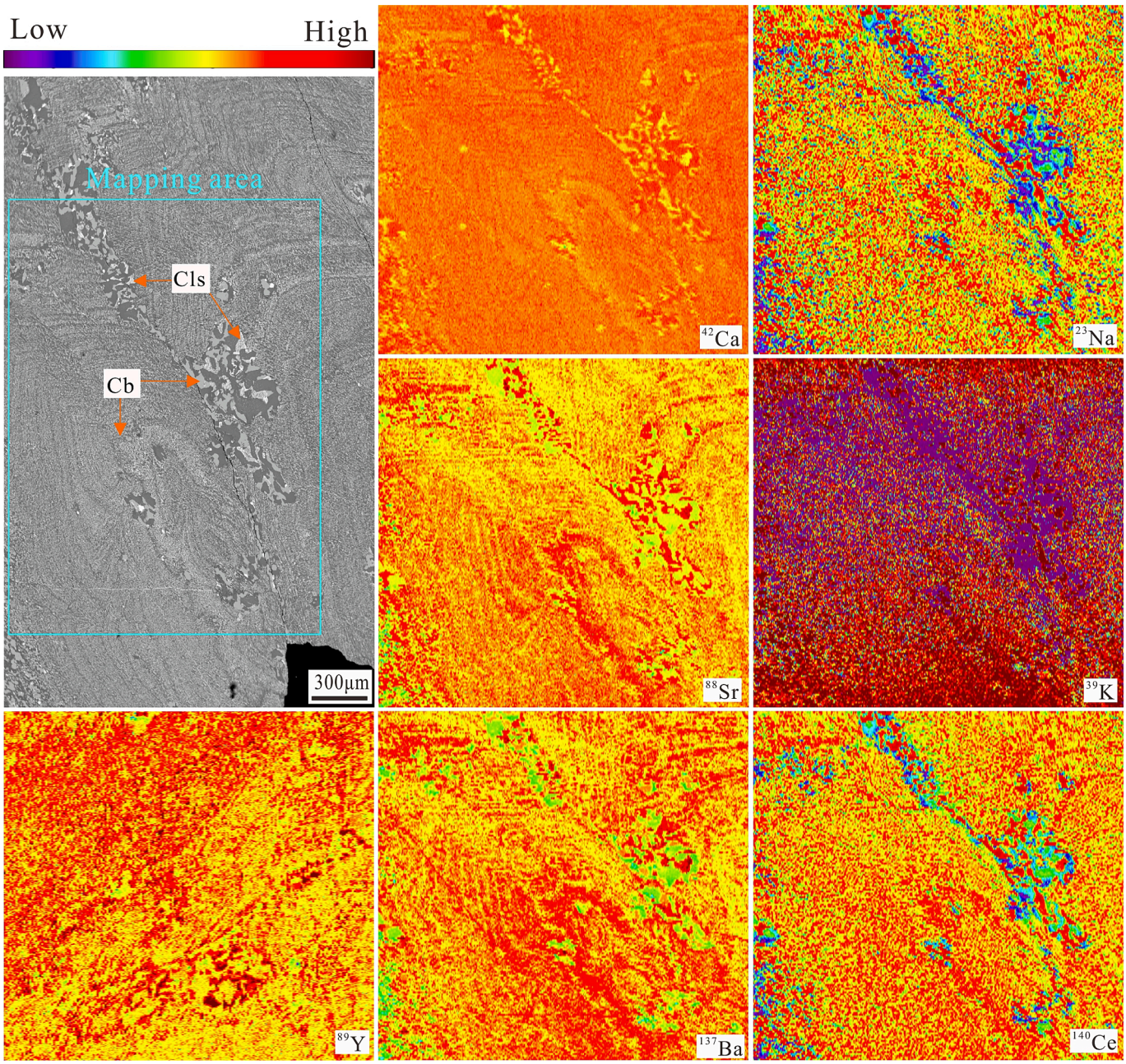

Fig. 9. LA-ICP-MS elemental mapping for a selected area in Cal-1 from the Weishan REE deposit.

(Yang et al., 2019b), the calculated $(^{87}Sr/^{86}Sr)_i$ and $\varepsilon_{Nd}(t)$ values are 0.707330–0.707854 and −15.8–−5.8 for Cal-1, 0.707771–0.708276 and −13.5–−8.0 for Cal-2, 0.707514–0.708275 and −12.4–−6.2 for Cal-3, and 0.707525–0.708974 and −16.1–−13.0 for Cal-4, respectively. Generally, the Cal-4 has the highest $(^{87}Sr/^{86}Sr)_i$ and lowest $\varepsilon_{Nd}(t)$ values (Fig. 10a).

4.4. C–O isotopic compositions of calcite

The $\delta^{13}C_{PDB}$ and $\delta^{18}O_{SMOW}$ values of the studied calcites range from −7.8‰ to −5.7‰ and 6.8‰ to 8.5‰, respectively. Specifically, the $\delta^{13}C_{PDB}$ and $\delta^{18}O_{SMOW}$ values are −7.4–−7.2‰ and 7.1–8.5‰ for Cal-1, −7.8–−5.6‰ and 6.8–7.9‰ for Cal-2, −7.6–−6.4‰ and 7.2–8.2‰ for Cal-3, and −7.6–−7.2‰ and 7.1–7.5‰ for Cal-4, respectively (Supplementary Table S4). There are no significant differences in $\delta^{13}C_{PDB}$ and $\delta^{18}O_{SMOW}$ values among the different stages of calcite, although minor scattered values occur (Fig. 10b).

5. Discussion

5.1. Calcite records of magmatic-hydrothermal evolution

Calcite occurs constantly from the early to the late stages in the Weishan REE deposit (Fig. 3). Both magmatic and hydrothermal origins have been proposed for the calcite (e.g., Lan et al., 2011b; Liang et al., 2017; Wang et al., 2019; Jia and Liu, 2020), of which the former is always controversial due to the lack of typical carbonatite veins. Four stages of calcite were identified in this study (Fig. 4), which show some differences in geochemistry, especially between the Cal-1 and the others (Fig. 8). However, the four stages of calcite have largely overlapped Sr-Nd and C-O isotopic compositions (Fig. 10), implying that they might be derived from the same source. The scattered Sr-Nd isotopic compositions

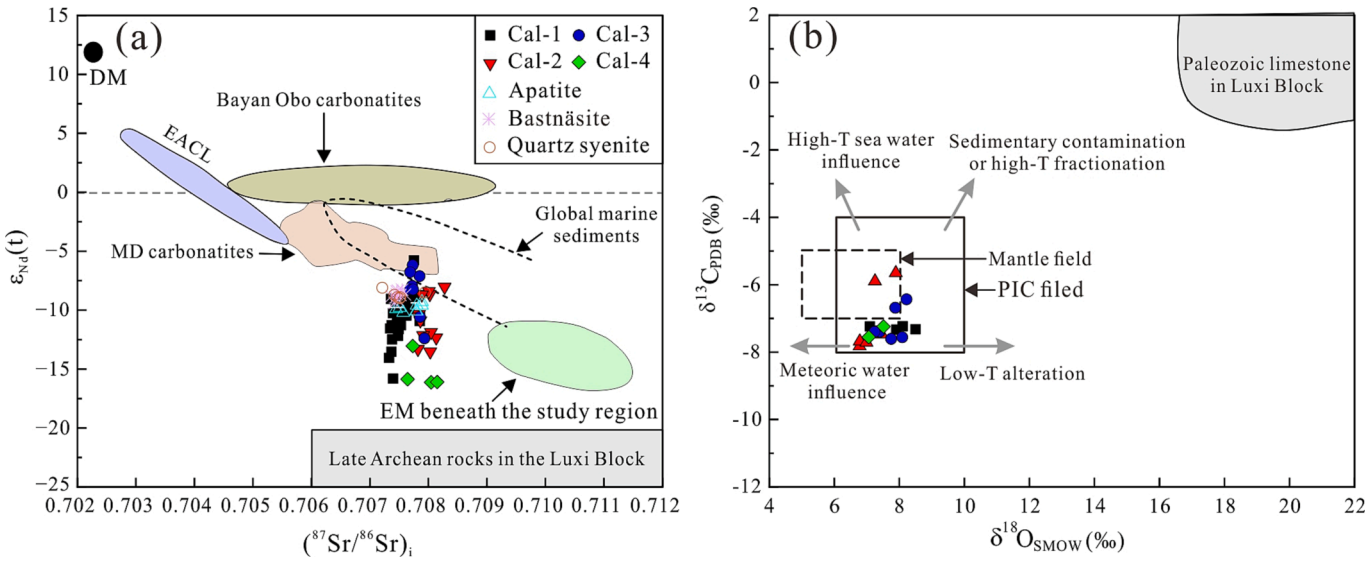

Fig. 10. Sr-Nd (a) and C-O (b) isotopic compositions for different stages of calcite from the Weishan REE deposit. In (a), the Sr-Nd isotopic compositions of bastnäsite (Lan et al., 2011b; Yang et al., 2019b), quartz syenite (Ding et al., 2022) and apatite in quartz syenite (Zeng et al., 2022) are shown for comparison. The areas of carbonatites from Bayan Obo and Mianning-Dechang (MD), depleted mantle (DM), East African Carbonatite Line (EACL) and global marine sediments are modified after Hou et al. (2015) and references therein. The late Archean rocks of Luxi Block (John et al., 1988) and enriched lithospheric mantle (EM) beneath the study region (Lan et al., 2019) are used to represent the crust and mantle endmembers in the study region. In (b), the C-O isotopic compositions of different endmembers and trends are modified after Demény et al. (1998). The area of Paleozoic limestones in Luxi Block (Liu et al., 2004) is shown for comparison.

show trend to the late Archean basement rocks (Fig. 10a), indicating the contamination from wallrocks or fluid-rock interaction. The uncontaminated Sr-Nd isotopic compositions resemble or even overlap with those of the alkaline rocks in the ore district (Fig. 10a). This suggests that the calcites or their related fluids were genetically associated with the alkaline rocks, which might be derived from the alkaline magmas.

The Cal-1 is characterized by exsolution of carbocernaite along its cleavage fractures with highest Na, K, Sr, Ba and REE contents (Fig. 5b, 6 and 8). Exsolution of carbocernaite has been identified in the calcite of carbonatite dyke from the Rajasthan, India, which was considered to be crystallized at the late stage of carbonatite magma (Wall et al., 1993). Actually, exsolution of minerals (e.g., carbocernaite, fluorite or fluorapatite) widely occurs in magmatic carbonates (e.g., Dawson et al., 1996; Potter et al., 2017; Anenburg and Mavrogenes, 2018). This implies that the Cal-1 might also form at the magmatic condition. The elemental compositions of Cal-1 support its affinity to the magmatic calcite. The remarkably high Sr (>60000 ppm), Ba (>7000 ppm) and LREE (>5000 ppm) contents of the Cal-1 are consistent with many igneous carbonatites worldwide (Yang and Le Bas, 2004; Xu et al., 2010; Chakhmouradian et al., 2016; Chen et al., 2020b). In the discrimination diagram of Yb/Ca vs. Yb/La (atom ratio) for magmatic and hydrothermal calcite, the spots of the Cal-1 are mainly plotted into the field of magmatic calcite (Fig. 11). In the other discrimination diagrams for selected magmatic, hydrothermal and sedimentary calcites, the spots of the Cal-1 are also plotted closely to the magmatic endmember (Fig. 12). Therefore, both the microtextural and elemental features of the Cal-1 indicate its magmatic origin. For the Cal-2, Cal-3 and Cal-4, they show evolutional features from the magmatic calcite (Fig. 11), but are plotted closely to the hydrothermal calcite (Figs. 11 and 12). Combined with their petrographic features and mineral assemblages, they should be classified as hydrothermal calcite.

Based on the above results, it is concluded that the calcites in the Weishan REE deposit transformed from magmatic to hydrothermal features with a continuous change. Because they show close spatio-temporal relationships with those of the alkaline silicate rocks in the ore district (Fig. 2), combined with their consistent isotopic compositions (Fig. 10a), it is inferred that the calcites were originally derived from the alkaline magmas. Carbonatitic melts coupled with abundant fluids can be exsolved from alkaline magmas (Nabyl et al., 2020; Walter et al., 2021), of which the carbonatitic melts crystallizing at the early stage resulted in the formation of Cal-1 while the fluids evolved to precipitate the Cal-2, Cal-3 and Cal-4 subsequently.

5.2. Exsolution and transportation of REE

Immiscibility between carbonate and silicate melts has been proposed for the generation of carbonatites and REE deposits in the carbonatite-alkaline silicate rock associations (Nabyl et al., 2020 and references therein). However, when and how the immiscibility processes occur were not well understood. Recent studies found that the enrichment of REE in the immiscible carbonate melts is highly associated with the degree of fractionation of the parental alkaline magma, showing that phonolitic/phono-trachytic melt compositions (e.g., SiO_2 contents of 58–64 wt% and $Na_2O + K_2O$ contents of 12–16 wt%) are the most favorable (Nabyl et al., 2020). In the Weishan REE deposit, the associated alkaline silicate rocks are mainly the quartz syenite, which has the SiO_2, Al_2O_3, Na_2O, K_2O and CaO contents of 62.0–71.7 wt%, 13.5–16.1 wt%, 5.53–7.13 wt%, 3.34–5.35 wt% and 0.37–1.59 wt%, respectively (Wei et al., 2019; Ding et al., 2022). These compositions are generally consistent with the compositions favorably generating the immiscible REE-rich carbonate melts, but are more acidic. This indicates that the separation of carbonate melts from the silicate melts probably occurred lately or shallowly during the magmatic evolution. The above inference can be supported by the widespread potassic (e.g., K-feldspar and muscovite) rather than sodic metasomatism in the Weishan REE deposit (Fig. 3a and 5a). Sodic metasomatism is commonly considered to form earlier, at higher temperatures and deeper levels than potassic metasomatism due to the higher mobility of K than Na at lower temperatures (Le Bas, 2008; Elliott et al., 2018). In addition, it has been found that fluid boiling widely occurred in the Weishan REE deposit (Li et al., 2009; Lan et al., 2011b), further supporting the exsolution of carbonate melts at shallow levels. The shallow exsolution could be more favorable for hydrothermal activity, as indicated by the widespread hydrothermal veins but less magmatic calcite (the scale of Cal-1 is small) in the ore district.

It has been revealed that LREE prefers to enter into the carbonate

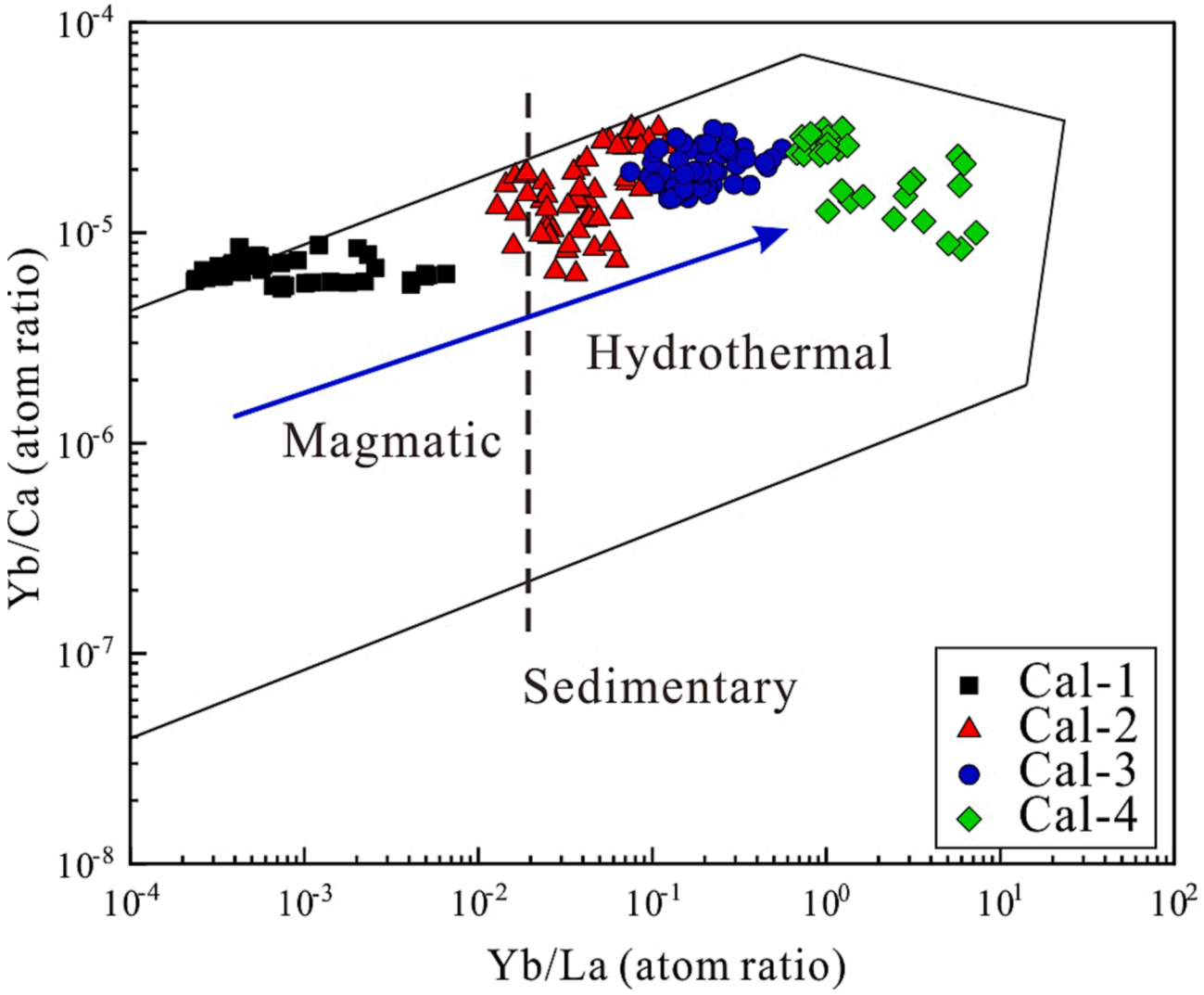

Fig. 11. Discrimination diagram for magmatic, hydrothermal and sedimentary calcite using Yb/Ca vs. Yb/La (atom ratio) (modified after Möller and Morteani, 1983).

melts relative to the silicate melts during immiscibility, especially under the H_2O– and alkalis-rich conditions (Martin et al., 2013; Nabyl et al., 2020). The Cal-1 in this study has the highest LREE contents (Fig. 6), corroborating the above conclusion. However, it is noted that the LREE minerals (e.g., bastnäsite and parisite) dominantly precipitated at the Cal-3 rather than the Cal-1 and Cal-2 stages. This means that the LREE was mainly kept in the fluids during the Cal-1 and Cal-2 stages, and thus should be complexed or aided by other ligands to retain in the fluids until the Cal-3 stage. Experimental studies show that alkalis (e.g., Na and K) can enhance the mobility of REE in carbonatitic systems, leading to the REE being efficiently transported from the melts into the fluids or being transported farther (Anenburg et al., 2020). The Cal-1 has the highest Na and K contents (Fig. 8a, b), indicating that alkalis were enriched in the early stage and thus might promote the LREE transportation. This can be supported by the consistent distributions between the alkalis and the LREE in the Cal-1 (Fig. 9). In addition, recent studies show that hydroxyl-carbonate complexes of REE such as $[REE_3(CO_3)_2(OH)_4(H_2O)_{12}]^+$ and $[REE_3(CO_3)_3(H_2O)_{12}]^{3+}$ can be formed in the alkaline fluids and enhance the mobility of REE, especially for the LREE at $T > 400$ °C (Louvel et al., 2022). In summary, the alkalis might have played an important role in LREE exsolution from the melts. This is meaningful because it can well explain why the LREE mineralization strongly occurred in the Weishan carbonatite-alkaline complexes while the contemporaneous (118–122 Ma) alkali-depleted carbonatite dykes in the Laiwu-Zibo area of the Luxi Block are ore-barren (Ying et al., 2004).

All kinds of ligands, such as Cl^-, F^-, CO_3^{2-} and SO_4^{2-}, have been proposed for the transportation of REE in hydrothermal fluids (Haas et al., 1995; Migdisov et al., 2016; Cui et al., 2020; Wan et al., 2021, 2023). In the Weishan REE deposit, carbonates, sulfates, fluorides and chlorides (e.g., halite and sylvite) occur either as ore-forming minerals or as daughter minerals in fluid inclusions (Li et al., 2009; Lan et al., 2011b), implying that the ore-forming fluids were enriched in the above ligands. However, fluoride has been proved to be the dominant REE depositional ligand in hydrothermal fluids (Migdisov et al., 2016), as also supported by the fluorite co-precipitating with REE minerals in the Cal-3 stage. Carbonate might promote the exsolution of REE at the early stage when coupled with alkalis (Louvel et al., 2022), but the strong deposition of calcite at the Cal-2 stage did not lead to the significant precipitation of REE, indicating that the carbonate complexes were not the critical transporting ligands of REE in the fluids. Based on comprehensive experimental and thermodynamic studies, Migdisov et al. (2016) concluded that chloride and sulfate complexes are the dominant REE transporting ligands in hydrothermal fluids. Recent studies corroborate that sulfate has enhanced solubility in hydrothermal fluids and elevated capability of transporting REE at the presence of quartz or alkalis (Cui

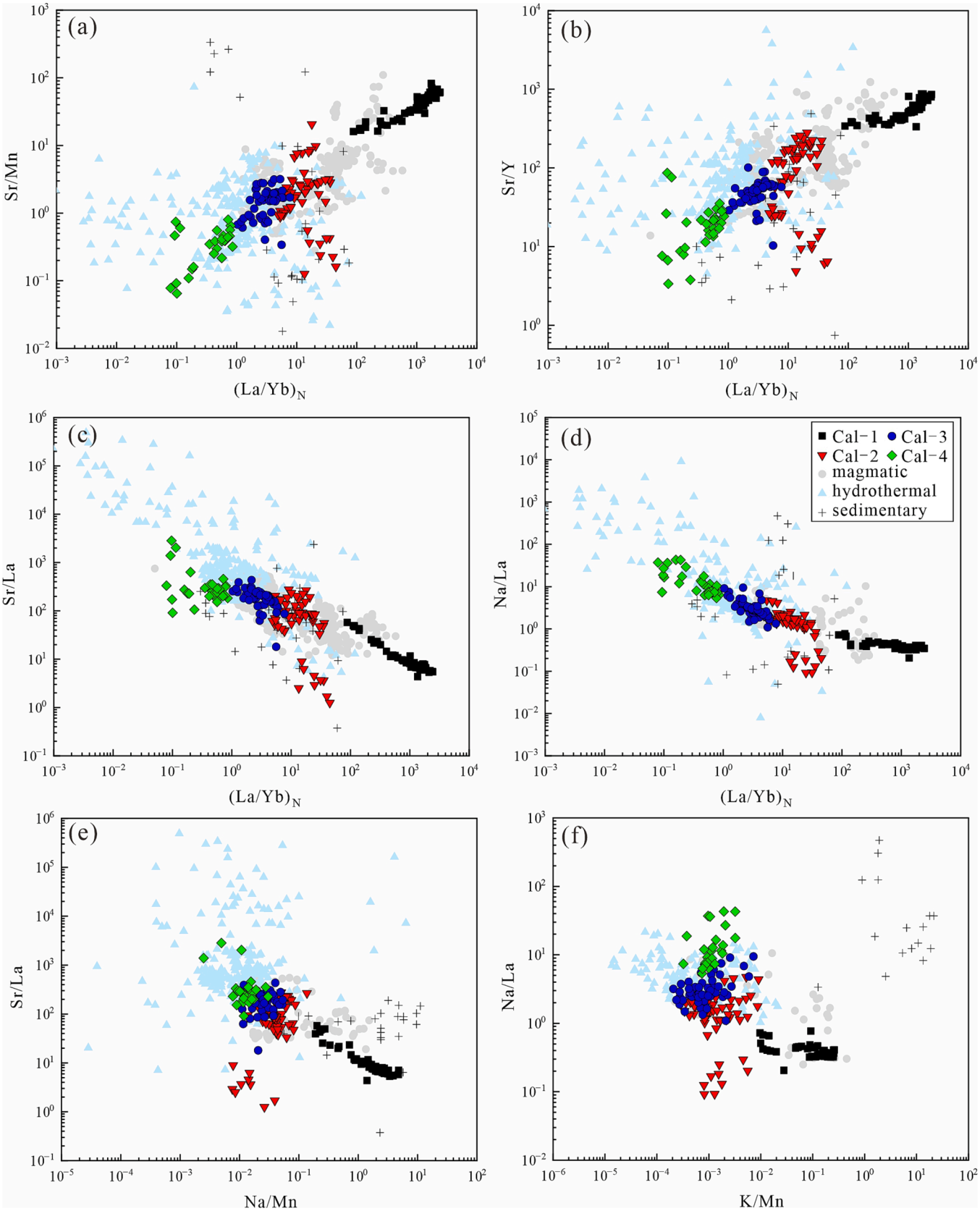

Fig. 12. Covariant plots of Sr/Mn vs. $(La/Yb)_N$ (a), Sr/Y vs. $(La/Yb)_N$ (b), Sr/La vs. $(La/Yb)_N$ (c), Na/La vs. $(La/Yb)_N$ (d), Sr/La vs. Na/Mn (e) and Na/La vs. K/Mn (f) for discriminating the genetic types of the studied calcites. Representative calcites from magmatic (Ionov and Harmer, 2002; Dawson and Hinton, 2003; Xu et al., 2008; Chen et al., 2011; Chakhmouradian et al., 2016; Song et al., 2017; Milani et al., 2017; Yang et al., 2019a; Castillo-Oliver et al., 2020; Ying et al., 2020; Baioumy, 2021), hydrothermal (Liu et al., 2019; Wellnitz et al., 2019; Zhuo et al., 2019; Castillo-Oliver et al., 2020; Ying et al., 2020; Gao et al., 2021; He et al., 2021; Jin et al., 2021) and sedimentary (Bolhar et al., 2015; Mirza et al., 2021; This study, Supplementary Table S2) origins are shown for comparison.

et al., 2020; Chen et al., 2020a, 2021; Wan et al., 2021, 2023). In the Weishan REE deposit, quartz and sulfates are abundant, of which the sulfates massively deposited at the Cal-2 stage and co-precipitated with REE minerals at the Cal-3 stage. This indicates decomposition of REE-sulfate complexes contributing to the precipitation of REE. Therefore, sulfate might be the dominant transporting ligand of REE.

5.3. Deposition and fractionation of REE

Decrease of temperature and pressure, fluid-rock interaction and change in redox condition can result in the REE precipitation (Williams-Jones et al., 2012; Migdisov et al., 2016; Wan et al., 2023). In the Weishan REE deposit, the REE minerals mainly precipitated at the Cal-3 stage, which were co-precipitated with all kinds of minerals such as fluorite, calcite, monazite, barite and so on (Figs. 3 and 4). This means that most of the anionic ligands (e.g., F^-, CO_3^{2-}, PO_4^{3-} and SO_4^{2-}) were destabilized at this stage. Because the Sr-Nd and C-O isotopic compositions from the Cal-1 to the Cal-3 stage do not change significantly (Fig. 10), fluid-rock interaction or external involvement might contribute little to the REE precipitation. This conclusion is also supported by the distinct boundaries between the ore veins and the wall-rocks (Fig. 3a, b). The S-bearing minerals occurred as sulfates in the Cal-2 and Cal-3 stages, but changed to sulfides in the Cal-4 stage, indicating that redox condition might keep stable from the Cal-2 to the Cal-3 stage but become more reduced in the Cal-4 stage. The change of oxygen fugacity thus could not play a significant role in REE precipitation.

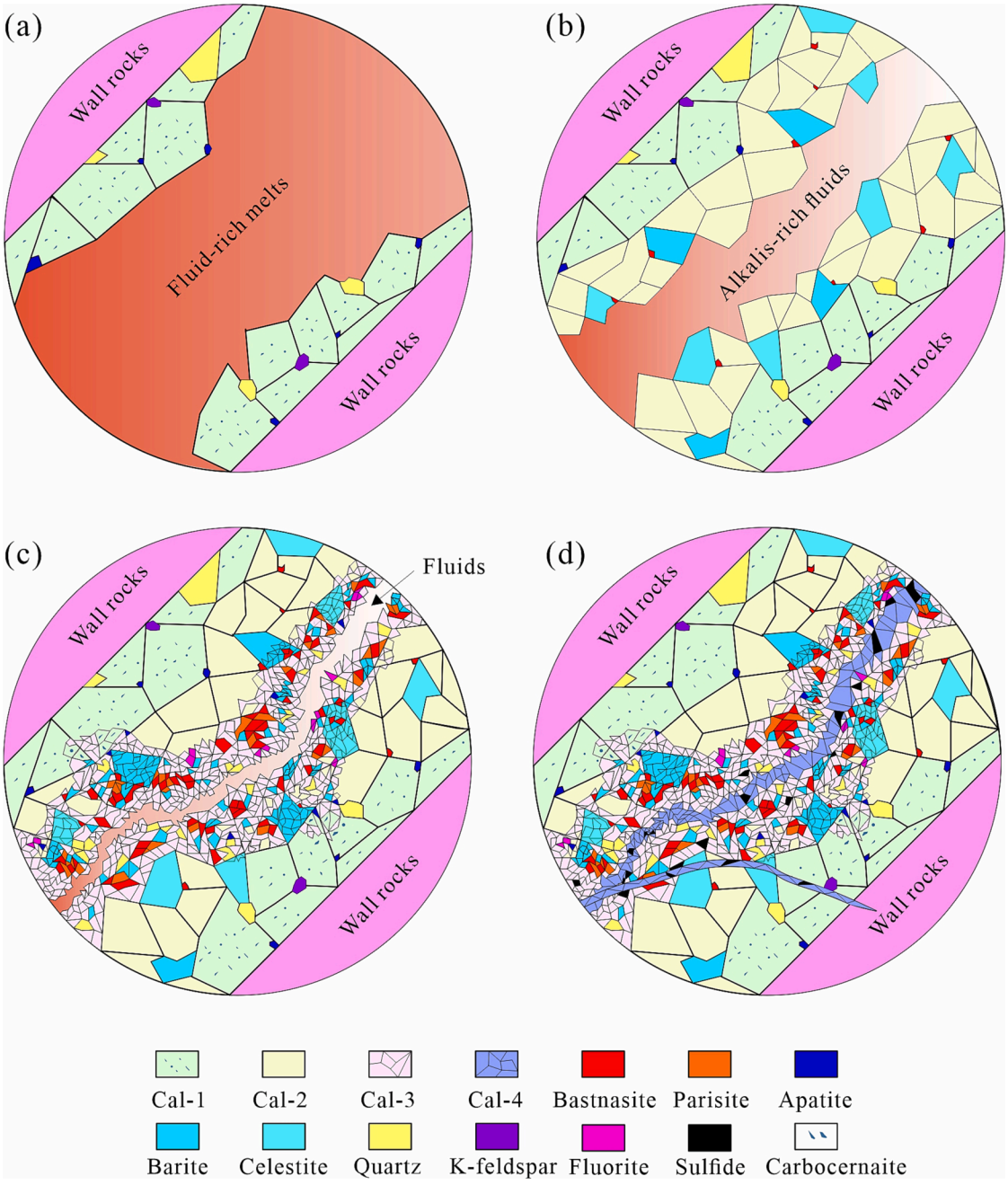

Fig. 13. Cartoons illustrating the formation of different stages of calcite and associated minerals in the Weishan REE deposit. (a) Crystallization of Cal-1 in fluid-rich carbonate melts with exsolution of carbocernaite. (b) Precipitation of Cal-2 from alkalis-rich fluids, co-precipitating with abundant sulfates (e.g., barite and celestite). (c) Co-precipitation of Cal-3 and REE minerals (e.g., bastnäsite and parisite) with abundant other minerals. (d) Precipitation of Cal-4 and sulfides, occurring as veinlets.

Actually, previous studies on fluid inclusions show that fluid boiling strongly occurred in the Weishan REE deposit, especially during the deposition of the REE minerals (Li et al., 2009; Lan et al., 2011b). Under this condition, the coupled decrease of temperature and pressure can significantly reduce the stability of the REE-sulfate complexes (Migdisov et al., 2016; Cui et al., 2020; Wan et al., 2021), resulting in the focused REE precipitation.

It is noted that from the Cal-1 to the Cal-4 stage the LREE contents of calcite decrease continuously while the HREE contents change slightly, leading to the decreasing fractionation between the LREE and the HREE (Fig. 7). Fractionation between LREE and HREE has been numerously studied, which can be attributed to their different mobilities and solubilities in melts, fluids and minerals (Migdisov et al., 2016 and references therein). It has been proven that LREE is more partitioned into carbonate melts than HREE during the carbonate–silicate melt immiscibility (Martin et al., 2013; Nabyl et al., 2020). The high LREE contents and $(La/Yb)_N$ ratios in the Cal-1 thus can be resulted from the above process. Actually, the associated alkaline silicate rocks in the Weishan REE deposit are also enriched in LREE with high $(La/Yb)_N$ ratio (Wei et al., 2019; Ding et al., 2022), which might further enhance the enrichment of LREE in the Cal-1 due to the inherence from the parental magmas. During subsequent hydrothermal evolution, LREE minerals such as bastnäsite and parisite precipitated, which strongly scavenged the LREE from the fluids, leading to the decrease of LREE in the co-precipitating calcite. By contrast, the HREE was more soluble than LREE in the alkalis-rich hydrothermal fluids (Anenburg et al., 2020), keeping in the fluids until the late hydrothermal stage. The different behaviors of the LREE and HREE thus balanced their contents in the fluids, resulting in the decreasing fractionation in calcite from the early to the late stages.

5.4. Genetic model of the REE mineralization

The elemental and isotopic compositions of calcite suggest that the ore-forming materials of the Weishan REE deposit were originally derived from the alkaline magmas. LREE-rich carbonate melts coupled with abundant alkaline fluids were exsolved from the alkaline magmas at shallow depth, leading to the formation of magmatic calcite at the early stage and hydrothermal calcite at the subsequent hydrothermal evolution (Fig. 13). The REE minerals mainly precipitated at the Cal-3 stage, at which time the REE-sulfate complexes were destabilized due to fluid boiling. This deposit shows significant hydrothermal features with poorly-developed carbonatites, distinct from the typical carbonatite-related REE deposits in the other places. The REE mineralization is thus considered to be basically controlled by the alkaline magmas rather than the carbonatites.

The isotopic compositions of ores and associated alkaline rocks in the Weishan REE deposit show affinities to the enriched lithospheric mantle (EM) beneath the study region, but are characterized by higher Nd and lower Sr isotopic values (Fig. 10a). This means that more depleted materials or deeper mantle materials were involved into the magma source (Zeng et al., 2022). The genesis of the EM beneath the study region has been numerously studied, which suggests that the mantle was strongly metasomatized by the subducted Yangtze continental crust during the early Mesozoic, leading to the enriched features with crust-like isotopic compositions (Zheng et al., 2018). Since the Jurassic, the EM was subducted by the Paleo-Pacific oceanic plate (Zhu and Xu, 2019; Wu et al., 2019), and was metasomatized by the carbonatic melts/fluids released from the slab (Zong and Liu, 2018), leading to the formation of REE-rich carbonated EM. During the early Cretaceous (~145–125 Ma), rollback of the subducted Paleo-Pacific plate occurred, resulting in the remarkable upwelling of the asthenospheric mantle and thus partial melting of the enriched lithospheric mantle (Zheng et al., 2018; Zhu and Xu, 2019). This generated the CO_2- and REE-rich alkaline magmas (Fig. 14). Notably, the Weishan REE deposit is the only economic REE deposit in the Luxi Block, which might be attributed to the favorable location controlled by the deeply-seated Tanlu fault (Fig. 2).

6. Conclusions

In-situ textural, elemental and isotopic analyses of calcite from the Weishan REE deposit were conducted to decipher the magmatic-hydrothermal evolution and the mineralization mechanisms of REE, leading to the following major conclusions:

(1) Four stages of calcite (Cal-1, Cal-2, Cal-3 and Cal-4) occurred in the Weishan REE deposit, of which the Cal-1 was magmatic while the others were hydrothermal, indicating the continuous magmatic-hydrothermal evolution.
(2) The LREE was dominantly transported as REE-sulfate complexes in the fluids, deposition of which was mainly induced by fluid boiling.
(3) From the early to the late stages, the LREE and HREE in calcite show a decreasing fractionation, which was resulted from the

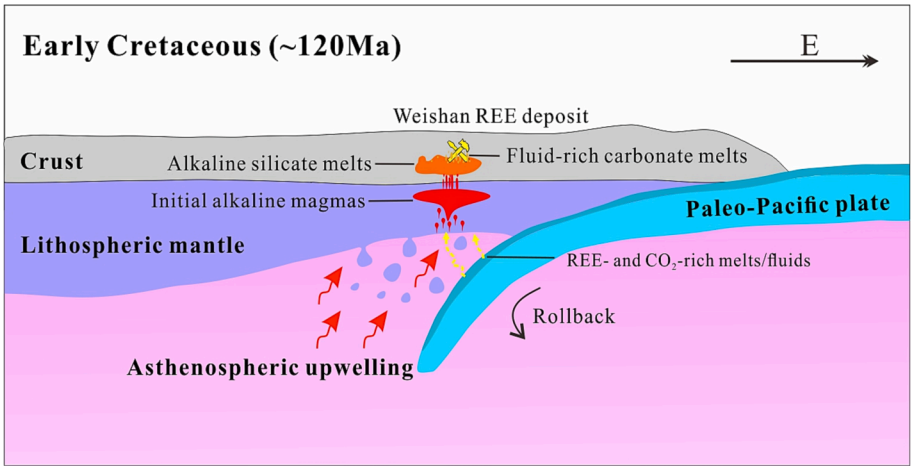

Fig. 14. A schematic model for the generation of the Weishan REE deposit. The lithospheric mantle beneath the study region was metasomatized by the subducted Paleo-Pacific oceanic slab since the Jurassic, becoming a REE-rich carbonated mantle. During the early Cretaceous, rollback of the subducted Pacific Plate occurred, leading to the remarkable asthenospheric upwelling and thus partial melting of the metasomatized mantle. The CO_2- and REE-rich alkaline magmas were generated through the above processes, exsolution of carbonate melts and abundant alkaline fluids from which occurred at relatively shallow depth. Continuous evolution of the exsolved materials led to the sequential crystallization/precipitation of magmatic and hydrothermal calcite and REE minerals. See details in the context.

deposition of LREE minerals, indicating the significant effects of hydrothermal processes on REE fractionation.

(4) The ore-forming materials were exsolved from alkaline magmas at relatively shallow depth, which had been originally derived from an enriched lithospheric mantle metasomatized by subducted oceanic slab.

Declaration of Competing Interest

The authors declare that they have no known competing financial interests or personal relationships that could have appeared to influence the work reported in this paper.

Data availability

Data will be made available on request.

Acknowledgements

We are grateful to Shaohua Dong, Wenqin Zheng, Xiang Li, Yun Li, Yanwen Tang, Junjie Han, Zhihui Dai, Xue Zhang and Dan Chen for their kind supports in analytical experiments. This study was financially supported by the National Natural Science Foundation of China (Grant NO. 41930430 and 42103069) and the West Light Foundation of Chinese Academy of Sciences (Grant No. xbzg-zdsys-202108).

Appendix A. Supplementary data

Supplementary data to this article can be found online at https://doi.org/10.1016/j.oregeorev.2023.105676.

References

Anenburg, M., Mavrogenes, J.A., 2018. Carbonatitic versus hydrothermal origin for fluorapatite REE-Th deposits: Experimental study of REE transport and crustal "antiskarn" metasomatism. Am. J. Sci. 318 (3), 335–366.

Anenburg, M., Mavrogenes, J.A., Frigo, C., Wall, F., 2020. Rare earth element mobility in and around carbonatites controlled by sodium, potassium, and silica. Sci. Adv. 6, eabb6570.

Baioumy, H., 2021. Geochemistry and origin of high-Sr carbonatite from the Nuba Mountains, Arabian-Nubian Shield, Sudan. J. Asian Earth Sci. 214, 104773.

Bolhar, R., Hofmann, A., Siahi, M., Feng, Y.X., Delvigne, C., 2015. A trace element and Pb isotopic investigation into the provenance and deposition of stromatolitic carbonates, ironstones and associated shales of the similar to 3.0 Ga Pongola Supergroup, Kaapvaal Craton. Geochim. Cosmochim. Acta 158, 57–78.

Castillo-Oliver, M., Giuliani, A., Griffin, W.L., O'Reilly, S.Y., Drysdale, R.N., Abersteiner, A., Thomassot, E., Li, X.H., 2020. New constraints on the source, composition, and post-emplacement modification of kimberlites from in situ C-O-Sr-isotope analyses of carbonates from the Benfontein sills (South Africa). Contrib. Miner. Petrol. 175, 33.

Chakhmouradian, A.R., Reguir, E.P., Couëslan, C., Yang, P., 2016. Calcite and dolomite in intrusive carbonatites. II. Trace-element variations. Mineralogy and Petrology 110 (2-3), 361–377.

Chen, H., Cui, H., Zhong, R.C., Xie, Y.L., Ye, C., Li, Z.M., Ling, Y.F., 2020a. Solubility of Na_2SO_4 in silica-saturated solutions: Implications for REE mineralization. Am. Mineral. 105, 1686–1694.

Chen, L.u., Liu, Y., Hu, Z., Gao, S., Zong, K., Chen, H., 2011. Accurate determinations of fifty-four major and trace elements in carbonate by LA-ICP-MS using normalization strategy of bulk components as 100%. Chem. Geol. 284 (3-4), 283–295.

Chen, W., Lu, J., Jiang, S.Y., Ying, Y.C., Liu, Y.S., 2018. Radiogenic Pb reservoir contributes to the rare earth element (REE) enrichment in South Qinling carbonatites. Chem. Geol. 494, 80–95.

Chen, W., Liu, H.-Y., Lu, J., Jiang, S.-Y., Simonetti, A., Xu, C., Zhang, W., 2020b. The formation of the ore-bearing dolomite marble from the giant Bayan Obo REE-Nb-Fe deposit, Inner Mongolia: insights from micron-scale geochemical data. Miner. Deposita 55 (1), 131–146.

Chen, L., Zheng, T., Xu, W., 2006. A thinned lithospheric image of the Tanlu Fault Zone, eastern China: constructed from wave equation based receiver function migration. J. Geophys. Res. Solid Earth 111, B09312.

Chen, H., Zhong, R., Xie, Y., Cui, H., Yu, C., Ling, Y., Li, Z., Li, L., 2021. Solubility of K_2SO_4 in silica-saturated solutions and applications to determine the composition of ore-forming fluids. Chem. Geol. 580, 120387.

Coplen, T.B., Kendall, C., Hopple, J., 1983. Comparison of stable isotope reference samples. Nature 302 (5905), 236–238.

Cui, H., Zhong, R., Xie, Y.L., Yuan, X.Y., Liu, W.H., Brugger, J., Yu, C., 2020. Forming sulfate- and REE-rich fluids in the presence of quartz. Geology 48, 145–148.

Dawson, J.B., Hinton, R.W., 2003. Trace-element content and partitioning in calcite, dolomite and apatite in carbonatite, Phalaborwa, South Africa. Mineral. Mag. 67 (5), 921–930.

Dawson, J.B., Pyle, D.M., Pinkerton, H., 1996. Evolution of natrocarbonatite from a wollastonite nephelinite parent: evidence from the June 1993 eruption of Oldoinyo Lengai, Tanzania. J. Geol. 104 (1), 41–54.

Demény, A., Ahijado, A., Casillas, R., Vennemann, T.W., 1998. Crustal contamination and fluid/rock interaction in the carbonatites of Fuerteventura (Canary Islands, Spain): a C, O, H isotope study. Lithos 44 (3-4), 101–115.

Ding, C., Zhao, B., Dai, P., Li, D., Zhang, Z., Sun, R., Wei, P., Liu, Q.i., Li, D., 2022. Geochronology, geochemistry and Sr–Nd–Pb–Hf isotopes of the alkaline–carbonatite complex in the Weishan REE deposit, Luxi Block: Constraints on the genesis and tectonic setting of the REE mineralization. Ore Geol. Rev. 147, 104996.

Elliott, H.A.L., Wall, F., Chakhmouradian, A.R., Siegfried, P.R., Dahlgren, S., Weatherly, S., Finch, A.A., Marks, M.A.W., Dowman, E., Deady, E., 2018. Fenites associated with carbonatite complexes: A review. Ore Geol. Rev. 93, 38–59.

Fan, W.M., Zhang, H.F., Baker, J., Jarvis, K.E., Mason, P.R.D., Menzies, M.A., 2000. On and off the North China Craton: where is the Archaean keel? J. Petrol. 41, 933–950.

Gao, L.G., Chen, Y.W., Bi, X.W., Gao, J.F., Chen, W.T., Dong, S.H., Luo, J.C., Hu, R.Z., 2021. Genesis of carbonatite and associated U-Nb–REE mineralization at Huayangchuan, central China: Insights from mineral paragenesis, chemical and Sr-Nd-C-O isotopic compositons of calcite. Ore Geol. Rev. 138, 104310.

Haas, J.R., Shock, E.L., Sassani, D.C., 1995. Rare-earth elements in hydrothermal systems: Estimates of standard partial molal thermodynamic properties of aqueous complexes of the rare earth elements at high pressures and temperatures. Geochim. Cosmochim. Acta 59 (21), 4329–4350.

He, Z., Li, Z., Li, B.o., Chen, J., Xiang, Z., Wang, X., Du, L., Huang, Z., 2021. Ore genesis of the Yadu carbonate-hosted Pb–Zn deposit in Southwest China: Evidence from rare earth elements and C, O, S, Pb, and Zn isotopes. Ore Geol. Rev. 131, 104039.

Hou, Z.Q., Liu, Y., Tian, S.H., Yang, Z.M., Xie, Y.L., 2015. Formation of carbonatite-related giant rare-earth-element deposits by the recycling of marine sediments. Sci. Rep. 5, 10231.

Ionov, D., Harmer, R.E., 2002. Trace element distribution in calcite-dolomite carbonatites from Spitskop: inferences for differentiation of carbonatite magmas and the origin of carbonates in mantle xenoliths. Earth Planet. Sci. Lett. 198 (3-4), 495–510.

Jia, Y.H., Liu, Y., 2020. REE enrichment during magmatic–hydrothermal processes in carbonatite-related REE deposits: A case study of the Weishan REE deposit, China. Minerals 10, 25.

Jin, X.Y., Zhao, J.X., Feng, Y.X., Hofstra, A.H., Deng, X.D., Zhao, X.F., Li, J.W., 2021. Calcite U-Pb dating unravels the age and hydrothermal history of the giant shuiyindong carlin-type gold deposit in the golden triangle, south china. Econ. Geol. 116, 1253–1265.

John, B.M., Auvray, B., Shen, Q.H., Liu, D.Y., Zhang, Z.Q., Dong, Y.J., Ye, X.J., Zhang, Q. Z., Cornichet, J., Mace, J., 1988. Archean crustal evolution in China: the Taishan complex, and evidence for juvenile crustal addition from long-term depleted mantle. Precambr. Res. 38 (4), 381–403.

Lan, T.G., Fan, H.R., Hu, F.F., Tomkins, A.G., Yang, K.F., Liu, Y.S., 2011a. Multiple crust–mantle interactions for the destruction of the North China Craton: Geochemical and Sr–Nd–Pb–Hf isotopic evidence from the Longbaoshan alkaline complex. Lithos 122, 87–106.

Lan, T.G., Fan, H.R., Hu, F.F., Yang, K.F., Wang, Y., 2011b. Genesis of the Weishan REE deposit, Shandong Province: Evidences from Rb-Sr isochron age, LA-MC-ICP-MS Nd isotopic compositions and fluid inclusions. Geochimica 40, 428–442 (in Chinese with English abstract).

Lan, T.G., Fan, H.R., Santosh, M., Hu, F.F., Yang, K.F., Yang, Y.H., Liu, Y.S., 2012. Early Jurassic high-K calc-alkaline and shoshonitic rocks from the Tongshi intrusive complex, eastern North China Craton: Implication for crust–mantle interaction and post-collisional magmatism. Lithos 140–141, 183–199.

Lan, T.G., Hu, R.Z., Chen, Y.H., Wang, H., Tang, Y.W., Liu, L., 2019. Generation of high-Mg diorites and associated iron mineralization within an intracontinental setting: Insights from ore-barren and ore-bearing intrusions in the eastern North China Craton. Gondw. Res. 72, 97–119.

Le Bas, M.J., 2008. Fenites associated with carbonatites. Can. Mineral. 46 (4), 915–932.

Li, S.R., Santosh, M., 2014. Metallogeny and craton destruction: records from the North China Craton. Ore Geol. Rev. 56, 376–414.

Li, J.K., Yuan, Z.X., Bai, G., Chen, Y.C., Wang, D.H., Ying, L.J., Zhang, J., 2009. Ore-forming fluid evolvement and its controlling to REE (Ag) mineralizing in the Weishan deposit, Shandong. Mineral. Petrol. 29, 60–68 (in Chinese with English abstract).

Liang, Y.W., Lai, Y., Hu, H., Zhang, F., 2017. Zircon U-Pb ages and geochemical characteristics study of syenite from Weishan REE deposit, Western Shandong. Acta Scientiarum Naturalium Universitatis Pekinensi 53, 652–666 (in Chinese with English abstract).

Liu, Y., Chakhmouradian, A.R., Hou, Z., Song, W., Kynický, J., 2019. Development of REE mineralization in the giant Maoniuping deposit (Sichuan, China): insights from mineralogy, fluid inclusions, and trace-element geochemistry. Miner. Deposita 54 (5), 701–718.

Liu, J.M., Zhang, H.F., Sun, J.G., Ye, J., 2004. Geochemical research on C-O and Sr-Nd isotopes of mantle-derived rocks from Shandong Province, China. Sci. China. Ser. D Earth Sci. 47, 171–180.

Louvel, M., Etschmann, B., Guan, Q., Testemale, D., Brugger, J., 2022. Carbonate complexation enhances hydrothermal transport of rare earth elements in alkaline fluids. Nat. Commun. 13, 1456.

Lu, S., Zhao, G., Wang, H., Hao, G., 2008. Precambrian metamorphic basement and sedimentary cover of the North China Craton: a review. Precambr. Res. 160 (1-2), 77–93.
Martin, L.H.J., Schmidt, M.W., Mattsson, H.B., Guenther, D., 2013. Element partitioning between immiscible carbonatite and silicate melts for dry and H_2O-bearing systems at 1–3 GPa. J. Petrol. 54, 2301–2338.
Migdisov, A., Williams-Jones, A.E., Brugger, J., Caporuscio, F.A., 2016. Hydrothermal transport, deposition, and fractionation of the REE: Experimental data and thermodynamic calculations. Chem. Geol. 439, 13–42.
Milani, L., Bolhar, R., Frei, D., Harlov, D.E., Samuel, V.O., 2017. Light rare earth element systematics as a tool for investigating the petrogenesis of phoscorite-carbonatite associations, as exemplified by the Phalaborwa Complex, South Africa. Miner. Deposita 52 (8), 1105–1125.
Mirza, T.A., Karim, K.H., Ridha, S.M., Fatah, C.M., 2021. Major, trace, rare earth element, and stable isotope analyses of the Triassic carbonates along the northeastern Arabian Plate margin: a key to understanding paleotectonics and paleoenvironment of the Avroman (Biston) limestone formation from Kurdistan region, northeastern Iraq. Carbonates and Evaporites 36, 66.
Möller, P., Morteani, G., 1983. On the geochemical fractionation of rare earth elements during the formation of Ca-minerals and its application to problems of the genesis of ore deposits. In: Augustithis, S.S. (Ed.), The Significance of Trace Elements in Solving Petrogenetic Problems and Controversies. Theophrastus, Athens, pp. 747–791.
Nabyl, Z., Massuyeau, M., Gaillard, F., Tuduri, J., Iacono-Marziano, G., Rogerie, G., Le Trong, E., Di Carlo, I., Melleton, J., Bailly, L., 2020. A window in the course of alkaline magma differentiation conducive to immiscible REE-rich carbonatites. Geochim. Cosmochim. Acta 282, 297–323.
Paton, C., Hellstrom, J., Paul, B., Woodhead, J., Hergt, J., 2011. Iolite: Freeware for the visualisation and processing of mass spectrometric data. J. Anal. At. Spectrom 26, 2508–2518.
Potter, N.J., Kamenetsky, V.S., Simonetti, A., Goemann, K., 2017. Different types of liquid immiscibility in carbonatite magmas: A case study of the Oldoinyo Lengai 1993 lava and melt inclusions. Chem. Geol. 455, 376–384.
Qiu, J., Lo, C.H., McInnes, B.I.A., Zhou, J., 2000. Potash-rich magmatism and associated goldcopper mineralization in the Yishu deep fault zone and its vicinity, eastern China. Resour. Geol. 50, 269–280.
Ren, J., Tamaki, K., Li, S., Junxia, Z., 2002. Late Mesozoic and Cenozoic rifting and its dynamic setting in eastern China and adjacent areas. Tectonophysics 344 (3-4), 175–205.
Song, W.L., Xu, C., Chakhmouradian, A.R., Kynicky, J., Huang, K.J., Zhang, Z.L., 2017. Carbonatites of Tarim (NW China): First evidence of crustal contribution in carbonatites from a large igneous province. Lithos 282, 1–9.
Sun, S.S., McDonough, W.F., 1989. Chemical and isotopic systematics of oceanic basalts: implications for mantle composition and processes. Geol. Soc. Lond. Spec. Publ. 42 (1), 313–345.
Wall, F., Le Bas, M.J., Srivastava, R.K., 1993. Calcite and carbocernaite exsolution and cotectic textures in a Sr, REE-rich carbonatite dyke from Rajasthan, India. Mineral. Mag. 57 (388), 495–513.
Walter, B.F., Giebel, R.J., Steele-MacInnis, M., Marks, M.A.W., Kolb, J., Markl, G., 2021. Fluids associated with carbonatitic magmatism: A critical review and implications for carbonatite magma ascent. Earth Sci. Rev. 215, 103509.
Wan, Y., Chou, I.M., Wang, X., Wang, R., Li, X., 2023. Hydrothermal sulfate surges promote rare earth element transport and mineralization. Geology 51, 449–453.
Wan, Y.e., Wang, X., Chou, I.-M., Li, X., 2021. Role of sulfate in the transport and enrichment of REE in hydrothermal systems. Earth Planet. Sci. Lett. 569, 117068.
Wang, C., Liu, J., Zhang, H., Zhang, X., Zhang, D., Xi, Z., Wang, Z., 2019. Geochronology and mineralogy of the Weishan carbonatite in Shandong province, eastern China. Geosci. Front. 10 (2), 769–785.
Wang, J.F., Sun, M.T., Du, X.B., Gan, Y.J., Zhang, G.Q., Wang, Z.L., 2016. Geological characteristics and prospecting potentiality of Xishan rare earth deposit in Shandong Province. Shandong Land and Resources 32, 32–40 (in Chinese with English abstract).
Wei, P.F., Yu, X.F., Li, D.P., Liu, Q., Yu, L.D., Li, Z.S., Geng, K., Zhang, Y., Sun, Y.Q., Chi, N.J., 2019. Geochemistry, zircon U-Pb geochronology, and Lu–Hf isotopes of the Chishan alkaline complex, Western Shandong, China. Minerals 9, 293.
Wellnitz, A.K., Scott, J.M., Martin, C.E., Palin, J.M., Stirling, C.H., Reid, M.R., Wombacher, F., Craw, D., 2019. Carbonation reactions and coupled element and isotope redistribution during shallow crustal gold mineralisation, New Zealand. Miner. Deposita 54 (5), 743–760.
Weng, Z.H., Jowitt, S.M., Mudd, G.M., Haque, N., 2015. A detailed assessment of global rare earth element resources: Opportunities and challenges. Econ. Geol. 110, 1925–1952.
Williams-Jones, A.E., Migdisov, A.A., Samson, I.M., 2012. Hydrothermal mobilisation of the rare earth elements - a Tale of "Ceria" and "Yttria". Elements 8, 355–360.
Wu, F.Y., Yang, J.H., Xu, Y.G., Wilde, S.A., Walker, R.J., 2019. Destruction of the North China Craton in the Mesozoic. Annu. Rev. Earth Planet. Sci. 47, 173–195.
Xie, Y.L., Verplanck, P.L., Hou, Z.Q., Zhong, R.C., 2019. Rare earth element deposits in China: A review and new understandings. Econ. Geol. 22, 509–552.
Xu, C., Campbell, I.H., Kynicky, J., Allen, C.M., Chen, Y.J., Huang, Z.L., Qi, L., 2008. Comparison of the Daluxiang and Maoniuping carbonatitic REE deposits with Bayan Obo REE deposit, China. Lithos 106, 12–24.
Xu, C., Kynicky, J., Chakhmouradian, A.R., Campbell, I.H., Allen, C.M., 2010. Trace-element modeling of the magmatic evolution of rare-earth-rich carbonatite from the Miaoya deposit, Central China. Lithos 118, 145–155.
Yang, K.F., Fan, H.R., Pirajno, F., Li, X.C., 2019a. The Bayan Obo (China) giant REE accumulation conundrum elucidated by intense magmatic differentiation of carbonatite. Geology 47, 1198–1202.
Yang, X.M., Le Bas, M.J., 2004. Chemical compositions of carbonate minerals from Bayan Obo, Inner Mongolia, China: Implications for petrogenesis. Lithos 72, 97–116.
Yang, Y.H., Wu, F.Y., Yang, J.H., Chew, D.M., Xie, L.W., Chu, Z.Y., Zhang, Y.B., Huang, C., 2014. Sr and Nd isotopic compositions of apatite reference materials used in U-Th-Pb geochronology. Chem. Geol. 385, 35–55.
Yang, Y.H., Wu, F.Y., Li, Q.L., Rojas-Agramonte, Y., Yang, J.H., Li, Y., Ma, Y., Wen, X., Huang, C., Fan, H.R., et al., 2019b. In situ U-Th-Pb dating and Sr-Nd isotope analysis of bastnäsite by LA-(MC)-ICP-MS. Geostand. Geoanal. Res. 43, 543–565.
Ying, Y.C., Chen, W., Simonetti, A., Jiang, S.Y., Zhao, K.D., 2020. Significance of hydrothermal reworking for REE mineralization associated with carbonatite: Constraints from in situ trace element and C-Sr isotope study of calcite and apatite from the Miaoya carbonatite complex (China). Geochim. Cosmochim. Acta 280, 340–359.
Ying, J.F., Zhou, X.H., Zhang, H.F., 2004. Geochemical and isotopic investigation of the Laiwu-Zibo carbonatites from western Shandong Province, China, and implications for their petrogenesis and enriched mantle source. Lithos 75, 413–426.
Yu, X.F., Tang, H.S., Han, Z.Z., Li, C.Y., 2010. Geological characteristics and origin of rare earth elements deposits related with alkaline rock in the Chishan-Longbaoshan Area, Shandong Province. Acta Geol. Sin. 84, 407–417 (in Chinese with English abstract).
Zeng, X., Li, X.C., Fan, H.R., Lan, T.G., Lan, J., Su, J.H., Zhang, P., Yang, K., Zhao, X.F., 2022. Generation of REE-rich syenite-(carbonatite) complex through lithosphere-asthenosphere interaction: An in-situ Sr–Nd–O isotopic study of the Mesozoic Weishan pluton, Northern China. J. Asian Earth Sci. 230, 105191.
Zhai, M.G., Santosh, M., 2011. The early Precambrian odyssey of the North China Craton: A synoptic overview. Gondw. Res. 20, 6–25.
Zhang, P., Liu, S.S., Lan, J., Li, Y.X, Xing, N., Yang, Y.T., Liu, J.J., Liu, Y.K., Kang, Z.Q., Yang, F., 2023. Isotope chronology, petrogeochemistry and its genesis of Chishan REE deposit in Weishan County, Shandong Province. Journal of Guilin University of Technology, https://kns.cnki.net/kcms/detail//45.1375.N.20230224.1417.002.html (in Chinese with English abstract).
Zhang, H.F., Sun, M., Zhou, X.H., Ying, J.F., 2005. Geochemical constraints on the origin of Mesozoic alkaline intrusive complexes from the North China Craton and tectonic implications. Lithos 81, 297–317.
Zhang, X.M., Zhang, Y.Q., Ji, W., 2007. Fault distribution patterns of the Luxi Block, Shandong, and Mesozic sedimentary-magmatic-structural evolution sequence. Journal of Geomechanics 13, 163–172 (in Chinese with English abstract).
Zhang, Y.F., Zhang, P., Liu, J.J., Lan, J., Xing, N., 2022. New research process and prospecting of Chishan endogenetic light rare earth deposit in Weishan Country in Shandong Province. Shandong Land and Resources 38, 19–25 (in Chinese with English abstract)..
Zheng, Y.F., Xu, Z., Zhao, Z.F., Dai, L.Q., 2018. Mesozoic mafic magmatism in North China: Implications for thinning and destruction of cratonic lithosphere. Sci. China Earth Sci. 61, 353–385.
Zhu, R.X., Xu, Y.G., Zhu, G., Zhang, H.F., Xia, Q.K., Zheng, T.Y., 2012. Destruction of the North China Craton. Sci. China Earth Sci. 55, 1565–1587.
Zhu, R., Xu, Y.G., 2019. The subduction of the west Pacific plate and the destruction of the North China Craton. Sci. China Earth Sci. 62, 1340–1350.
Zhuo, Y.Z., Hu, R.Z., Xiao, J.F., Zhao, C.H., Huang, Y., Yan, J., Li, J.W., Gao, W., Li, J.X., 2019. Trace elements and C-O isotopes of calcite from Carlin-type gold deposits in the Youjiang Basin, SW China: Constraints on ore-forming fluid compositions and sources. Ore Geol. Rev. 113, 103067.
Zong, K.Q., Liu, Y.S., 2018. Carbonate metasomatism in the lithospheric mantle: Implications for cratonic destruction in North China. Sci. China Earth Sci. 61, 711–729.